

Absorption Lines in the 0.91–1.33 μm Spectra of Red Giants for Measuring Abundances of Mg, Si, Ca, Ti, Cr, and Ni

KEI FUKUE,¹ NORIYUKI MATSUNAGA,^{2,1} SOHEI KONDO,^{3,1} DAISUKE TANIGUCHI ,² YUJI IKEDA ,^{4,1}
NAOTO KOBAYASHI ,^{3,5,1} HIROAKI SAMESHIMA ,⁵ SATOSHI HAMANO ,⁶ AKIRA ARAI,¹ HIDEYO KAWAKITA,^{1,7}
CHIKAKO YASUI,^{6,1} MISAKI MIZUMOTO ,^{8,9} SHOGO OTSUBO,¹ KEIICHI TAKENAKA,⁷ TOMOHIRO YOSHIKAWA,¹⁰ AND
TAKUJI TSUJIMOTO ⁶

¹Laboratory of Infrared High-resolution spectroscopy (LiH), Koyama Astronomical Observatory,
Kyoto Sangyo University, Motoyama, Kamigamo, Kita-ku, Kyoto 603-8555, Japan

²Department of Astronomy, School of Science, The University of Tokyo, 7-3-1 Hongo, Bunkyo-ku, Tokyo 113-0033, Japan

³Kiso Observatory, Institute of Astronomy, School of Science, The University of Tokyo, 10762-30 Mitake, Kiso-machi, Kiso-gun, Nagano
397-0101, Japan

⁴Photocoding, 460-102 Iwakura-Nakamachi, Sakyo-ku, Kyoto 606-0025, Japan

⁵Institute of Astronomy, School of Science, The University of Tokyo, 2-21-1 Osawa, Mitaka, Tokyo 181-0015, Japan

⁶National Astronomical Observatory of Japan, 2-21-1 Osawa, Mitaka, Tokyo 181-8588, Japan

⁷Department of Physics, Faculty of Science, Kyoto Sangyo University, Motoyama, Kamigamo, Kita-ku, Kyoto 603-8555, Japan

⁸Department of Astronomy, Kyoto University, Kitashirakawa-Oiwake-cho, Sakyo-ku, Kyoto 606-8502, Japan

⁹Hakubi Center, Kyoto University, Yoshida-honmachi, Sakyo-ku, Kyoto 606-8501, Japan

¹⁰Edechs, 17203 Iwakura-Minami-Osagi-cho, Sakyo-ku, Kyoto 606-0003, Japan

(Received Month Day, 2020; Revised Month Day, Year; Accepted Month Day, Year)

Submitted to ApJS

ABSTRACT

Red giants show a large number of absorption lines in both optical and near-infrared wavelengths. Still, the characteristics of the lines in different wave passbands are not necessarily the same. We searched for lines of Mg I, Si I, Ca I, Ti I, Cr I, and Ni I in the z' , Y , and J bands (0.91–1.33 μm), that are useful for precise abundance analyses, from two different compilations of lines, namely, the third release of Vienna Atomic Line Database (VALD3) and the catalog published by Meléndez & Barbuy in 1999 (MB99). We selected sufficiently strong lines that are not severely blended and ended up with 191 lines (165 and 141 lines from VALD3 and MB99, respectively), in total, for the six elements. Combining our line lists with high-resolution ($\lambda/\Delta\lambda = 28,000$) and high signal-to-noise (> 500) spectra taken with the WINERED spectrograph, we measured the abundances of the six elements in addition to Fe I of two prototype red giants, i.e., Arcturus and μ Leo. The resultant abundances show reasonable agreements with literature values within ~ 0.2 dex, indicating that the available oscillator strengths are acceptable, although the abundances based on the two line lists show systematic differences by 0.1–0.2 dex. Furthermore, to improve the precision, solid estimation of the microturbulence (or the microturbulences if they are different for different elements) is necessary as far as the classical hydrostatic atmosphere models are used for the analysis.

Keywords: Spectroscopy (1558); High resolution spectroscopy (2096); Spectral line identification (2073); Spectral line lists (2082); Stellar spectral lines (1630); Late-type giant stars (908); Near infrared astronomy (1093)

1. INTRODUCTION

A list of stellar absorption lines, containing their information such as wavelengths and oscillator strengths, is essential in the analysis of chemical abundances. Com-

pared to established lists of lines in the optical, however, the identification and characterization of absorption lines in the near-infrared range remains incomplete (see, e.g., [Andreasen et al. 2016](#); [Matsunaga et al. 2020](#)). The correct identification of lines is mandatory, and estimating the abundances cannot be done accurately without accurate calibration of the oscillator strengths, $\log gf$ ¹.

We focus on stellar absorption lines in the $z'YJ$ bands, 0.91–1.33 μm , in this paper. In [Kondo et al. \(2019, hereafter referred to as Paper I\)](#), we identified 107 Fe I lines that are useful for measuring the iron abundances in the spectra of two well-studied red giants (Arcturus and μ Leo). While the iron abundance is one of the most representative parameters that indicates how stars are chemically enriched, the abundances of other elements provide us with crucial information on the evolution of the Milky Way and nearby galaxies ([Freeman & Bland-Hawthorn 2002](#); [Feltzing & Chiba 2013](#)). Following [Paper I](#), the purpose of the current study is to extend the identification of lines in the $z'YJ$ bands to other elements, namely, Mg I, Si I, Ca I, Ti I, Cr I, and Ni I. These elements show ~ 10 or more lines, as we see below, which would enable precise chemical measurements ([Adibekyan et al. 2015](#)).

In addition to the quality of the line list, the microturbulence, ξ , is a critical ingredient for performing abundance measurements. This parameter is not required as long as one deals with weak lines within the linear region of the curve of growth. However, in practice, stronger lines are often included in the analysis to secure a sufficient number of lines. The ξ is required to reproduce the saturated region of the curve of growth with classical 1D atmospheric models with the local thermodynamic equilibrium (LTE) assumed ([Gray 2005](#)), while 3D hydrodynamical models do not require ξ given as an external parameter ([Asplund 2000](#); [Amarsi et al. 2016](#)). The 3D models are also expected to include naturally the systematic effects caused by 3D/spherical structures in extended red giants ([Dobrovolskas et al. 2013](#)). Although the use of 3D hydrodynamical models has been gradually explored ([Jofré et al. 2019](#), and references therein), it is currently more common to use 1D models for the abundance analysis because it is easier to use and allows direct comparisons with previous results based on 1D models. In a classical approach with 1D models, a depth-independent ξ is estimated by demanding that the abundances estimated with individual lines show no dependency on line strengths, e.g., equivalent widths

(EWs, denoted as W) or reduced EWs (W/λ). This method requires many lines of the same element covering a wide range of strengths, and Fe I lines are most often used. In [Paper I](#), we performed a bootstrap analysis to determine ξ and its error by using more than 50 Fe I lines in the $z'YJ$ bands. Among the six elements we add in this paper, Si I and Ti I show many lines enough for doing the same analysis to determine ξ , and we compare the results obtained with these two elements with that obtained with Fe I.

2. SPECTRAL DATA AND LINE SELECTION

2.1. Observations and data

We investigate the same $z'YJ$ -band spectra used in [Paper I](#). The spectra of well-studied red giants (Arcturus and μ Leo) were collected with the WINERED cross-dispersed echelle spectrograph ([Ikeda et al. 2016](#)) with the WIDE mode, giving the resolution of $\lambda/\Delta\lambda = 28,000$. We carried out the observation on February 23, 2013, with the 1.3 m Araki Telescope at Koyama Astronomical Observatory, Kyoto Sangyo University, Japan (see more details in Table 1 of [Paper I](#)). The spectrum of a telluric standard, HIP 76267 (A1 IV), was used for the correction of telluric absorption lines with the method described in [Sameshima et al. \(2018\)](#). The wavelength ranges of the three bands in which the telluric lines can be well-corrected cover 0.91–0.93, 0.96–1.115, and 1.16–1.33 μm . The continuum of the spectra was normalized to the unity after the telluric correction. The signal-to-noise ratios (S/N) at around 12,500 Å are $\sim 1,000$ before the telluric correction and are 850 and 720 in the final spectra of Arcturus and μ Leo, respectively. The stellar redshifts were corrected so that the absorption lines can be directly compared with those in synthetic spectra in the wavelength scale of standard air at rest.

2.2. Line selection

We followed the procedure described in [Paper I](#) to select the absorption lines that are relatively isolated and useful for precise abundance measurements. The details that support the following brief description are given in [Paper I](#).

We used two line lists, Vienna Atomic Line Database (VALD3; [Ryabchikova et al. 2015](#)) and the list published by [Meléndez & Barbuy \(1999, hereafter referred to as MB99\)](#), as the starting points of the line selection. VALD3 has an extensive collection of atomic lines, e.g., including more than 10,000 Fe I lines, and molecular lines covering the wavelength range of the $z'YJ$ bands. In our spectrum of Arcturus, [Ikeda et al.](#) (in preparation) identified atomic lines of various species, including more than 300 lines of Fe I together with other elements

¹ Here and elsewhere in this paper, we consider only the logarithm to base 10.

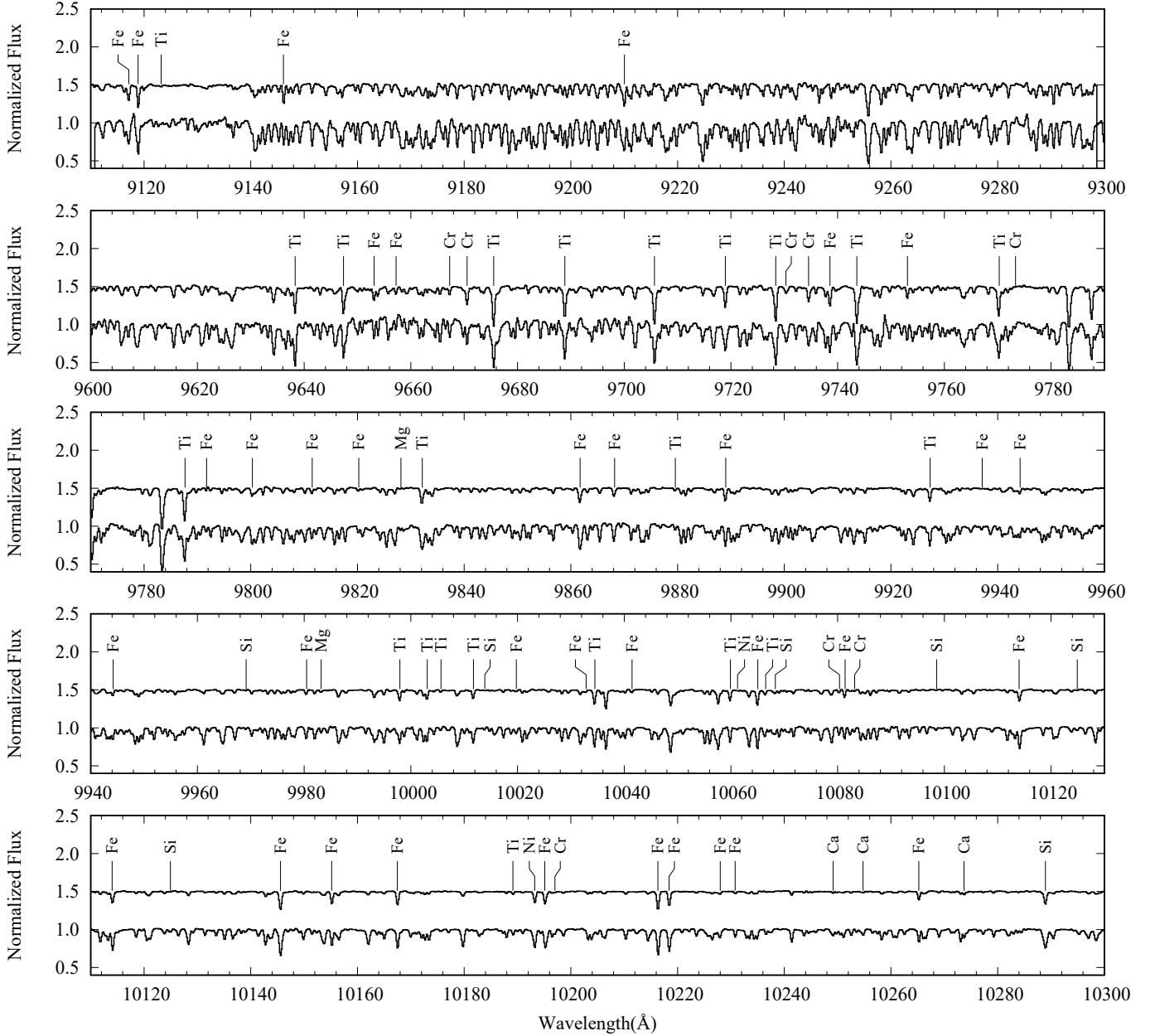


Figure 1. Selected absorption lines seen in Arcturus (upper) and/or μ Leo (lower). Their spectra are presented in the scale of wavelength in the standard air. Tables 1 and 2 give details of the lines selected from VALD3 and MB99, respectively.

(see a summary in Taniguchi et al. 2018, Section 3.2). MB99 used the solar spectrum for the line identification and the calibration of the $\log gf$ values, and compiled ~ 1000 atomic lines in $1.00\text{--}1.34\ \mu\text{m}$. The wavelength and the excitation potential (EP in eV) of each line are consistent between the two line lists, but the $\log gf$ values in the two lists tend to be significantly different. While we considered all the lines of the six elements in MB99 as candidates, the VALD3 lines detected by Ikeda et al. were included, rather than all the VALD3 lines, in the following analysis.

We performed the line selection for the six elements (Mg I, Si I, Ca I, Ti I, Cr I, and Ni I) making use of synthetic spectra except for the final confirmation with the observed spectra. In the following analysis, we used the stellar parameters adopted from Heiter et al. (2015) as we did in Paper I; the effective temperature (T_{eff}), the surface gravity ($\log g$), and the global metallicity ($[M/H]$) are 4279 ± 40 K, 1.60 ± 0.18 dex, and -0.51 ± 0.06 dex for Arcturus, and 4520 ± 43 K, 2.36 ± 0.22 dex, and $+0.33 \pm 0.06$ dex for μ Leo. The spectral synthesis was done with SPTOOL developed by Y. Takeda (private communication), which utilizes

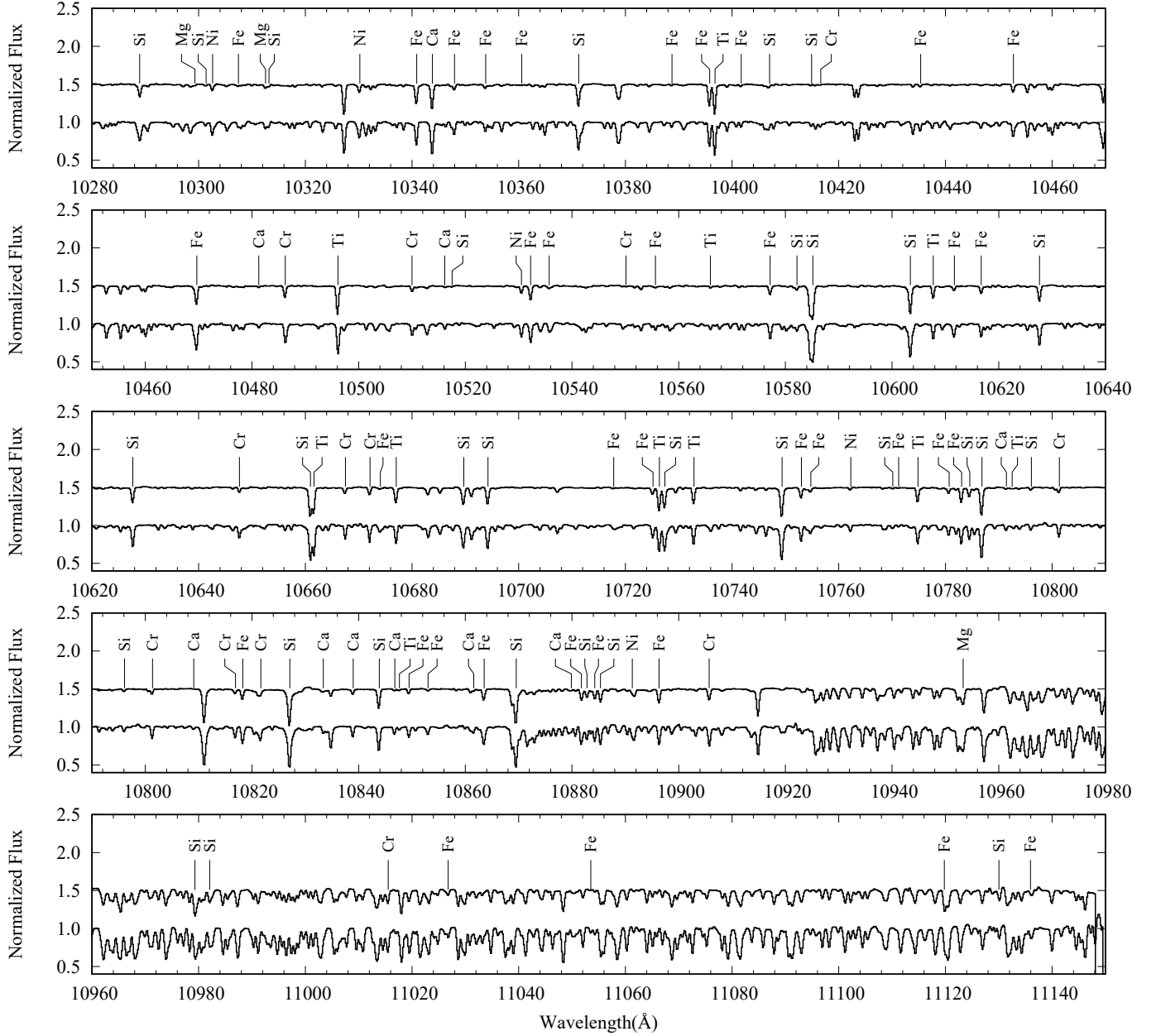


Figure 1. (Continued.)

the ATLAS9/WIDTH9 codes by R. L. Kurucz (Kurucz 1993). For each object, we considered two synthetic spectra for which the atomic lines of VALD3 or MB99 are considered (i.e., we avoided mixing atomic lines of the two lists in our spectral analysis). In both cases, we included lines of CN, CO, C₂, CH, and OH molecules using the list compiled by VALD3.

As the first step of the line selection, we excluded lines in the following three ranges, as they are severely affected by telluric lines: 9300–9600 Å, 11150–11600 Å, and longer than 13300 Å. Then, we measured the depths and central wavelengths of the lines in the synthetic

spectra for the two objects, Arcturus and μ Leo. If the depth of a line (the distance from the normalized continuum to the line minimum) was smaller than 0.03 in the synthetic spectra, the line was rejected. We also rejected lines with no minimum in the synthetic spectra for neither of the two objects within 5 km s⁻¹ around the expected wavelength. Besides, when two or more lines of the same element were detected within 30 km s⁻¹, we included only the strongest line if its X value was larger than those of the other neighboring line(s) by more than 0.5 dex; otherwise, we rejected all the lines in the narrow wavelength range. The X index is defined as

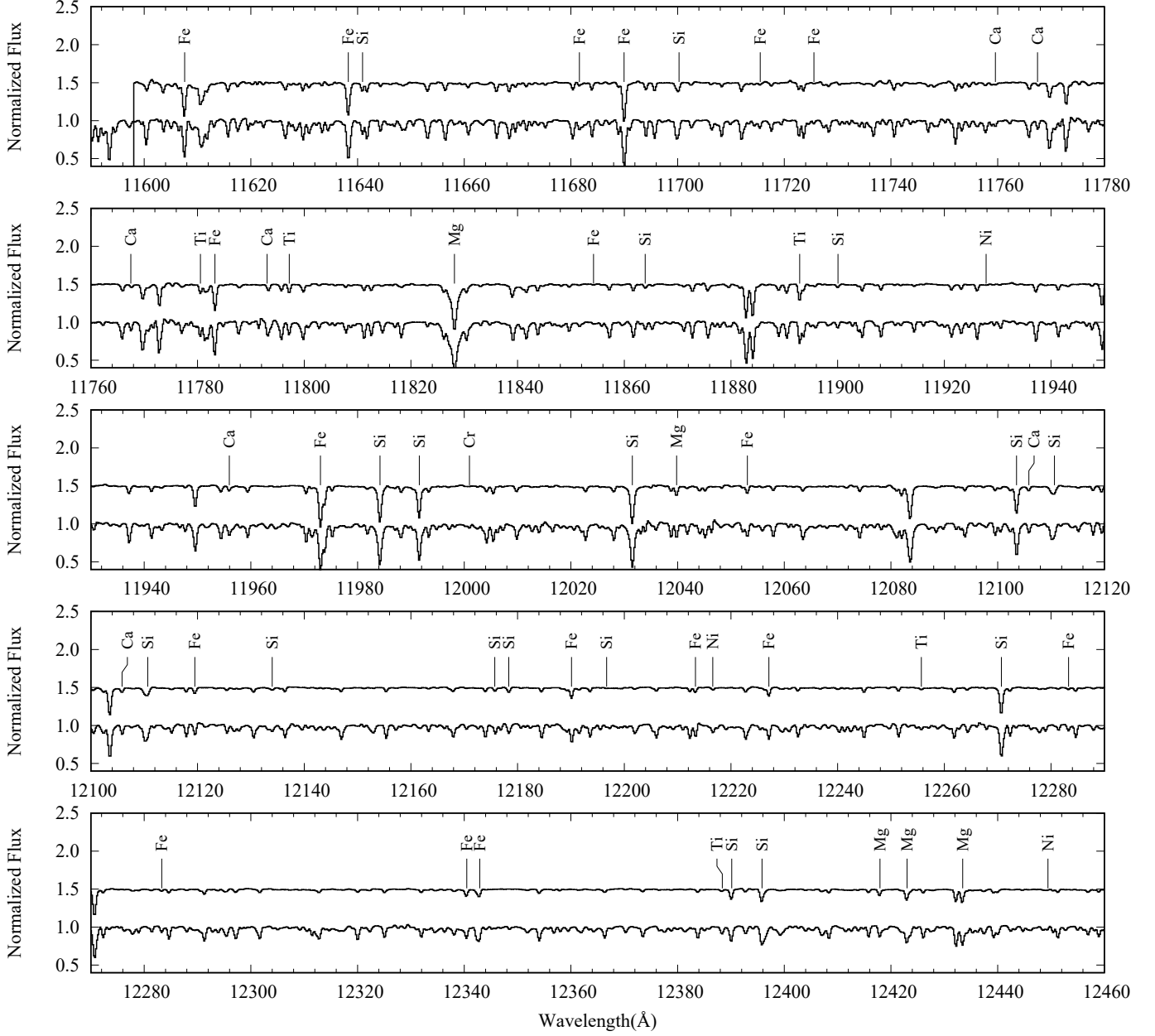


Figure 1. (Continued.)

$X \equiv \log gf - EP \times \theta_{\text{exc}}$, where $\theta_{\text{exc}} \equiv 5040 / (0.86 T_{\text{eff}})$. It is a convenient indicator of line strength (Magain 1984; Gratton et al. 2006). These rejections, and also those in the following steps, were made independently for each combination of the line list (VALD3 or MB99) and the object (Arcturus or μ Leo).

The next step is to evaluate the blending of each target line with neighboring lines based on a few types of theoretical EWs. We used two kinds of synthetic spectra generated for each target line, i.e., the normal spectrum with all the lines included, f_{syn} , and the one with the target line removed, f_{syn}^{\dagger} . A normal EW around a target

line (λ_c) is given by

$$W_i = \int_{\lambda_c - \Delta_i/2}^{\lambda_c + \Delta_i/2} \{1 - f_{\text{syn}}(\lambda)\} d\lambda, \quad (1)$$

and we considered two different integration ranges, Δ_1 and Δ_2 , that correspond to velocities of 30 and 60 km s⁻¹, respectively. In addition, we calculated the EW of contaminating lines, W_i^{\dagger} , which was estimated by Equation (1) but using f_{syn}^{\dagger} . Combining these EWs, we consider two indices,

$$\beta_1 = W_1^{\dagger} / W_1, \quad (2)$$

$$\beta_2 = (W_2^{\dagger} - W_1^{\dagger}) / W_1, \quad (3)$$

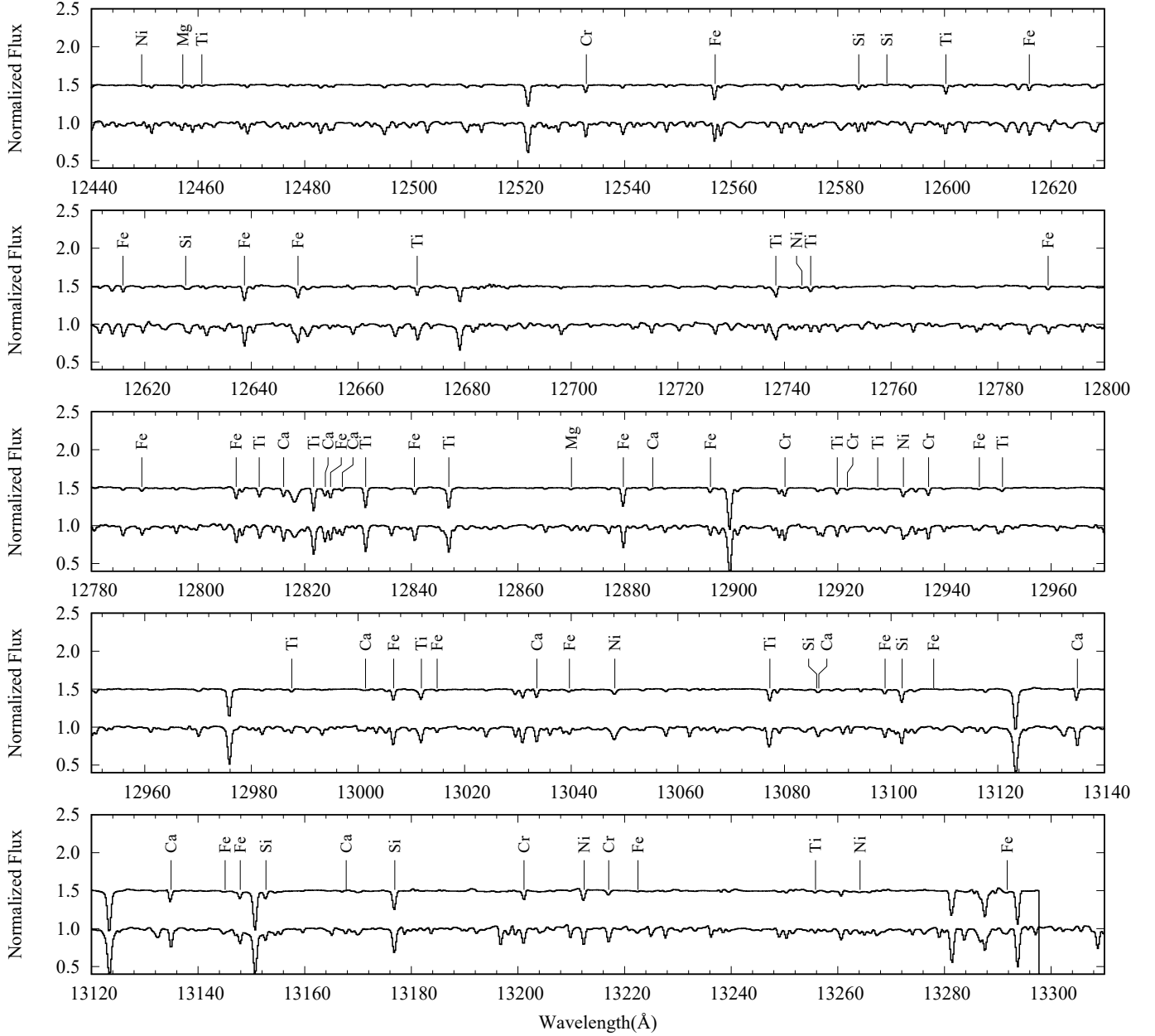


Figure 1. (Continued.)

as the indicators of blending. The former measures the contamination to the main part of each target line, and the latter measures the contamination mainly to the continuum part around the line. We rejected lines with $\beta_1 > 0.3$ or $\beta_2 > 1$ (see Figure 3 in Paper I for some examples with different β_1 and β_2 values). Finally, we examined whether the lines selected with the synthetic spectra exist in the observed spectra. We rejected Mg I 11820.982 (EP = 5.933, $\log gf = -1.520$) selected from VALD3, though not listed in MB99, because we could not confirm its absorption in the observed spectra.

From VALD3, we selected 12 lines for Mg I, 50 for Si I, 15 for Ca I, 50 for Ti I, 25 for Cr I, and 13 for Ni I (Table 1). From MB99, the numbers are slightly smaller except for Ca I: 8 for Mg I, 49 for Si I, 22 for Ca I, 34 for Ti I, 21 for Cr I, and 7 for Ni I (Table 2). For Fe I, 97 and 75 lines, respectively, from VALD3 and MB99 are adopted from Paper I and included in Tables 1 and 2. Some lines were selected only for one of the two objects owing to the large difference in metallicity; some lines were too weak in the metal-poor object, Arcturus, while some other lines were severely blended with neighboring lines in the metal-rich object, μ Leo. Figure 2 shows

Table 1. Lines Selected from VALD3 and Abundances

λ_{air} (Å)	Atom	EP (eV)	$\log gf$ (dex)	Arcturus (dex)	μ Leo (dex)	flag
9117.1309	Fe I	2.8581	-3.454	-0.37	+0.36	0/2
9118.8806	Fe I	2.8316	-2.115	(s)	(s)	0/0
9123.2029	Ti I	3.1129	-0.619	-0.38	-1.84:	1/2
9146.1275	Fe I	2.5881	-2.804	-0.61	-0.35	0/2
9210.0240	Fe I	2.8450	-2.404	-0.65	(s)	0/1
9602.1301	Fe I	5.0117	-1.744	(w)	+0.11	0/1
9638.3043	Ti I	0.8484	-0.612	(s)	(s)	0/0
9647.3700	Ti I	0.8181	-1.434	(s)	(s)	0/0
9653.1147	Fe I	4.7331	-0.684	-0.61	+0.31	0/2
9657.2326	Fe I	5.0856	-0.780	-0.65	-0.20	0/2

NOTE— This is the first 10 lines, and the entire list is available as an online material. The wavelengths, λ_{air} , are given on the standard air scale. The abundances, $[X/H]$, for Arcturus and μ Leo are scaled with respect to the solar abundance in [Grevesse et al. \(2007\)](#), but the flags, (w), (s), (b), or (*) are given if we did not measure the abundances. The last column gives the flag of outlier(s), and the colon symbol (:) accompanies the abundances that were judged as outliers. See Section 3.1 about the flags.

EPs and $\log gf$ values of the selected lines. The lines of different elements tend to have different EPs; for example, Si I have high EPs ($\gtrsim 5$ eV), Ti I have low EPs ($\lesssim 3$ eV), while the EPs of Fe I lines range from ~ 2 to ~ 6 eV. The summary of the line selection for individual elements are given in Appendix A.

3. ABUNDANCE ANALYSIS

3.1. Measurements of individual lines

We measured the abundance by fitting a small spectral part, within ± 30 km s $^{-1}$, around each target line using the MPFIT tool ([Takeda 1995](#)) implemented in SP-TOOL as we did in [Paper I](#), but we made some changes. This tool can search for the best match between synthetic and observational spectra by iteratively varying the abundance and some other parameters, including the line broadening width. However, unlike in [Paper I](#), we fixed the line broadening width of each spectrum to 13.3 km s $^{-1}$ for Arcturus and 12.0 km s $^{-1}$ for μ Leo, which we determined by measuring the widths of hundreds of lines of various elements. These widths correspond to the full-width at the half-maximum of each absorption line and include the broadenings intrinsic to the stellar line profile and the instrumental broadening. As a matter of fact, the instrumental broadening of the WINERED with the WIDE mode is 12 km s $^{-1}$, significantly larger than the macroturbulence of Arc-

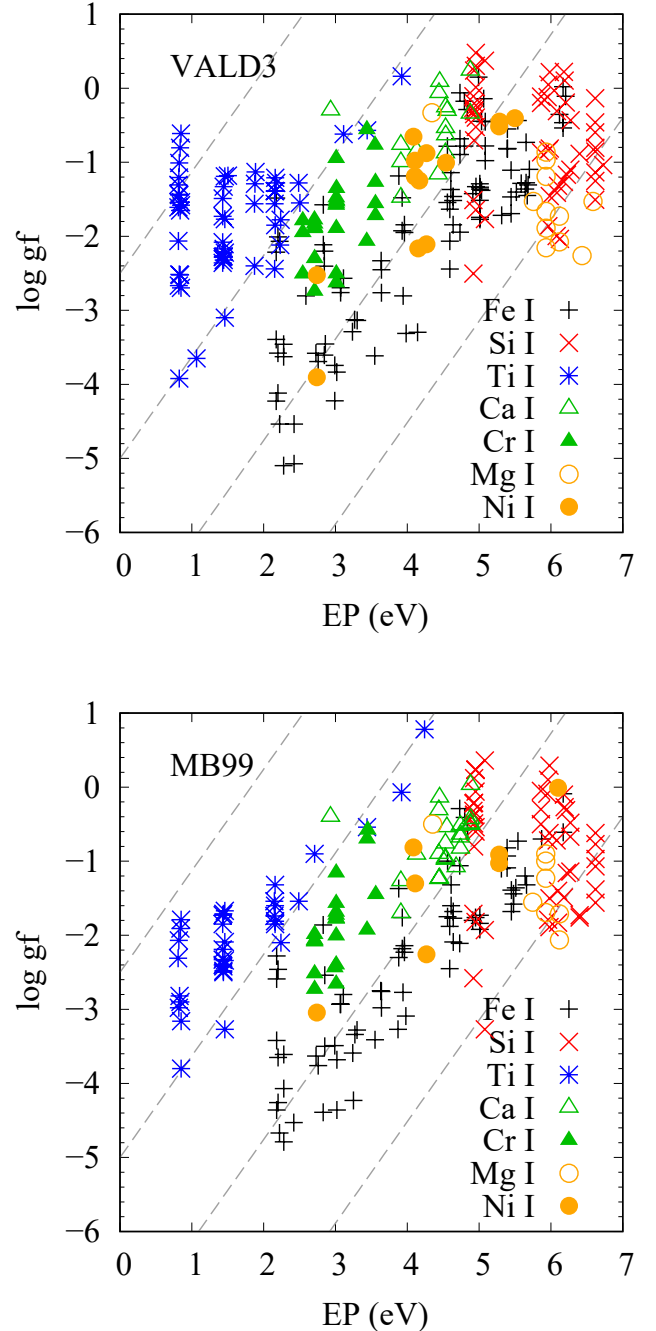


Figure 2. Excitation potential (EP) and the oscillator strength ($\log gf$) of the selected lines for six elements in addition to Fe. The lines selected from VALD3 (Table 1) and those from MB99 (Table 2) are presented in the upper and lower panels, respectively. The dashed lines show the contours of the X indicator, $\log gf - EP \times (5040 / (0.86 T_{\text{eff}}))$, for which T_{eff} of Arcturus (4286 K) is used. This indicator nicely predicts which lines are relatively strong (stronger towards the upper left corner) among each element, but the X scale differs from one element to another because it does not take the elemental abundances into account.

Table 2. Lines Selected from MB99 and Abundances

λ_{air} (Å)	Atom	EP (eV)	$\log gf$ (dex)	Arcturus (dex)	μ Leo (dex)	flag
10003.09	Ti I	2.16	-1.32	-0.21	+0.19	0/2
10011.74	Ti I	2.15	-1.54	-0.03	(b)	0/1
10013.86	Si I	6.40	-1.73	(w)	-0.17	0/1
10019.79	Fe I	5.48	-1.44	(w)	+0.30	0/1
10032.86	Fe I	5.51	-1.36	(w)	+0.26	0/1
10034.49	Ti I	1.46	-2.09	+0.12	+0.65	0/2
10041.47	Fe I	5.01	-1.84	(w)	+0.51	0/1
10059.90	Ti I	1.43	-2.40	+0.02	+0.54	0/2
10065.05	Fe I	4.84	-0.57	-0.25	+0.52	0/2
10066.55	Ti I	2.16	-1.85	-0.10	+0.47	0/2

NOTE— This is the first 10 lines, and the entire list is available as an online material. The wavelengths, λ_{air} , are given on the standard air scale. The abundances, $[X/H]$, for Arcturus and μ Leo are scaled with respect to the solar abundance in Grevesse et al. (2007), but the flags, (w), (s), or (b) are given if we did not measure the abundances. The last column gives the flag of outlier(s), and the colon symbol (:) accompanies the abundances that were judged as outliers. See Section 3.1 about the flags.

turus (5.59 km s^{-1} ; Sheminova 2015) and that of μ Leo (2.9 km s^{-1} ; Smith et al. 2013). The microturbulence, ξ , was fixed at each run of the MPFIT fitting, and we combined the measurements with different ξ to estimate it (Section 3.2). Besides, for the spectral synthesis with the MPFIT, we used the abundance patterns of iron and the six elements adopted from Jofré et al. (2015) and of CNO adopted from Smith et al. (2013) for each of our targets (Table 3). When we change the global metallicity, $[M/H]$, of an atmospheric model, we increase or decrease $[X/H]$ by the same amount and keep these patterns. This is different from the analysis of Paper I in which we used the solar abundance pattern taken from Anders & Grevesse (1989) for both Arcturus and μ Leo. Using the abundance pattern of each object in Table 3, instead of the solar pattern, leads to better reproduction of contaminating lines in each target’s spectrum. When we measure the abundance of a particular element X, in contrast, we change its $[X/H]$ but keep the abundances of all the other elements.

MPFIT gives the abundances in the form of $\log \epsilon(X) = \log N_X / \log N_H + 12$, where N_X indicates the number density of the element X. We transformed this form to $[X/H] = \log \epsilon(X) - \log \epsilon(X)_{\odot}$ for which we adopted the solar compositions reported by Grevesse et al. (2007) that are given in Table 4. The compositions of Grevesse

Table 3. The reference abundances, $\log \epsilon(X)$, used in the MPFIT analysis and as the zero points of $[X/H]$

Z	X	Sun (AG89)	Arcturus (G07)	μ Leo
6	C	8.56	8.39	7.96 (S13) 8.52 (S13)
7	N	8.05	7.78	7.64 (S13) 8.71 (S13)
8	O	8.93	8.66	8.64 (S13) 9.05 (S13)
12	Mg	7.58	7.53	7.56 (J15) 8.18 (J15)
14	Si	7.55	7.51	7.24 (J15) 8.02 (J15)
20	Ca	6.36	6.31	6.00 (J15) 6.58 (J15)
22	Ti	4.99	4.90	4.56 (J15) 5.22 (J15)
24	Cr	5.67	5.64	5.00 (J15) 5.93 (J15)
26	Fe	7.67	7.45	6.93 (J15) 7.70 (J15)
28	Ni	6.25	6.23	5.68 (J15) 6.52 (J15)

References— AG89 = Anders & Grevesse (1989); G07 = Grevesse et al. (2007); S13 = Smith et al. (2013); J15 = Jofré et al. (2015)

et al. (2007) were also used in Smith et al. (2013) and Jofré et al. (2015), with the results of which we compared our measurements below.

We did not measure the abundances for the lines that were expected to be too weak, depth smaller than 0.03, and for those expected to be too much blended on the basis of β_1 and β_2 . The former and latter cases are indicated by the flags (w) and (b), respectively, in Tables 1 and 2. Besides, we decided not to measure the abundance for the lines whose depth is more than 0.35 in the synthetic spectra; the flag of (s) is given to these cases. In Paper I, we used the threshold of $X = -6$ for Fe I lines for avoiding very strong lines. Since the X indices of different elements cannot be directly compared, we consider the depth for this selection, and 0.35 in depth roughly corresponds to $X = -6$ in the case of Fe I (Figure 3). Based on synthesized absorption lines of Si I and Ti I, we also confirmed that the damping wing becomes important at the depth of 0.35 or more, which is consistent with Fe I lines. We note that this threshold in depth depends on the spectral resolution because the resolution of the WINERED is not high enough to resolve the intrinsic line profile. We include the strong lines in our list for completeness and also because they are expected to be weaker in metal-poor stars.

While MPFIT failed in Paper I to measure the abundance of μ Leo with nine Fe I lines mainly because of unexpected blends of strong lines, we measured the abundances with those Fe I lines successfully for Arcturus and/or μ Leo in the new analysis except Fe I 11119.795

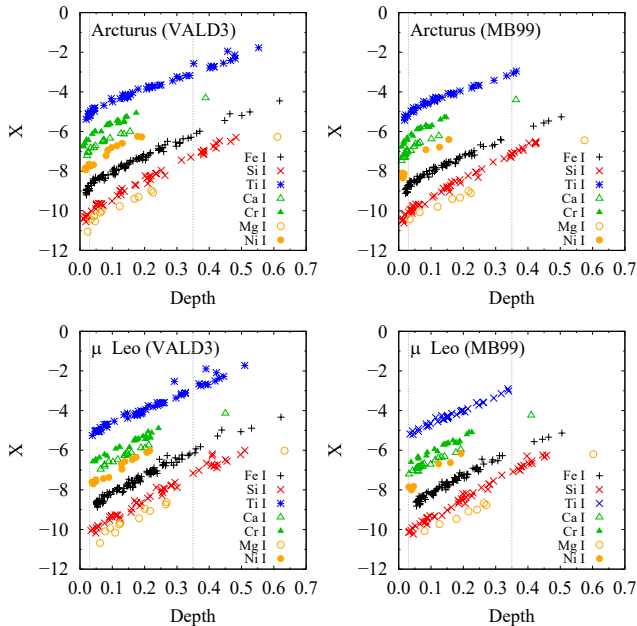


Figure 3. Relationship between the X indices and line depths in the synthetic spectra. This plot includes all the lines listed in Table 1 (for VALD3) and Table 2 (for MB99) regardless of whether they were selected or not for each object and whether their abundances were measured or not. The depths here include the absorption by contaminating lines if any. In our measurements, the ratio of equivalent width (EW) to depth is approximately 500 m\AA in the linear region ($\text{EW} \lesssim 50 \text{ m\AA}$), but the depth of 0.35 corresponds to $\text{EW} \approx 190 \text{ m\AA}$.

which is too strong in both objects. Some of the lines are contaminated by a neighboring line (or lines) that is not well reproduced in the synthetic spectra, but fixing the broadening widths helps to find reasonable fits to the target lines without being disturbed by the contaminated profile too much. On the other hand, we could not measure $[\text{Si}/\text{H}]$ of μ Leo with Si I 10407.037 which looks severely disturbed with the absorption at $\sim 10406 \text{ \AA}$ that are present in the observed spectrum but not predicted by the synthetic spectrum. The flag of (*) is given to this case in Table 1.

3.2. Microturbulence and its effects

In Paper I, we applied a bootstrap approach to Fe I lines to determine the depth-independent microturbulence (ξ) and the iron abundance at the same time. In this method, we measure the Fe I abundances with individual lines for a grid of ξ values. Generally speaking, the estimate of $[\text{X}/\text{H}]$ tends to decrease with increasing ξ except for shallow lines whose EWs do not depend on ξ . The deeper, more saturated lines have the stronger dependency on ξ . Deep lines give higher (or

lower) $[\text{X}/\text{H}]$ than shallow lines at a lower (higher) ξ . It is naively expected that $[\text{X}/\text{H}]$ values with strong/weak lines agree at the true ξ . We consider the linear relation, $[\text{X}/\text{H}] = aX + b$, where X is the line strength indicator (Section 2.2), to represent the dependency of $[\text{X}/\text{H}]$ on line strength. The relation, in particular its slope, changes with varying ξ . A common approach for estimating ξ is to find ξ that gives $a = 0$ (see, e.g., Blackwell & Willis 1977; de Jager et al. 1984, for slightly different approaches). With the method in Paper I, we generate bootstrapping samples of the lines, each of which has a sequence of $(\xi, [\text{X}/\text{H}])$ values, and determine ξ together with $[\text{X}/\text{H}]$ for each bootstrapping sample repeatedly. Then, we evaluate the best estimates of the $(\xi, [\text{X}/\text{H}])$ of the star and their errors considering the distribution on the ξ - $[\text{X}/\text{H}]$ plane given by the bootstrapping samples.

Since we made some changes in measuring the abundances of individual lines (Section 3.1), we performed the bootstrap analysis on Fe I lines again. The resultant ξ and $[\text{Fe}/\text{H}]$, listed in Table 4, are consistent with the previous values in Paper I within uncertainties, but the errors get slightly smaller. In addition, we made the same analysis for Si I and Ti I. Among the elements we investigate, beside Fe I, the numbers of only Si I and Ti I lines are large enough for the bootstrap analysis for determining ξ together with the abundance. As shown in Table 4 and Figure 4, the ξ obtained for Si and Ti lines tend to be higher than those for Fe lines.

We performed the same bootstrap analysis for subsets of the Fe I, Si I, and Ti I lines to which we could apply the non-LTE correction. Bergemann et al. (2012, 2013) carried out non-LTE line formation calculations in the atmospheres of red supergiants for Fe, Ti, and Si, and discussed the consequences of non-LTE effects for the J -band analysis. It was found that non-LTE effects are small for J -band Fe I lines, but significant for Ti I and Si I lines. We calculated the non-LTE corrections on the lines of Fe I, Si I, and Ti I using their website². Their online tool gives the non-LTE corrections for the abundances obtained with individual lines for a given set of stellar parameters. We added the corrections to $[\text{X}/\text{H}]$ with individual VALD3 lines, and performed the same bootstrapping analysis, but with smaller numbers of lines, to calculate ξ and $[\text{X}/\text{H}]$. Not all the lines we selected are included in their tool, but dozens of the lines could be included in this analysis. Table 4 and Figure 4 present the resultant ξ and $[\text{X}/\text{H}]$. In the case of Arcturus, ξ gets slightly higher, but the non-LTE cor-

² <http://nlte.mpia.de/gui-siuAC.secE.php>

Table 4. Microturbulences and Abundances Obtained with Fe, Si, and Ti Lines

Atom	List	NLTE	N	ξ (km s^{-1})	$[X/H]$ (dex)	r
<i>Arcturus</i>						
Fe I	MB99	—	53	$1.25^{+0.08}_{-0.08}$	$-0.45^{+0.03}_{-0.03}$	-0.872
Fe I	VALD	—	66	$1.28^{+0.14}_{-0.12}$	$-0.65^{+0.06}_{-0.06}$	-0.949
Fe I	VALD	NLTE	47	$1.42^{+0.21}_{-0.19}$	$-0.69^{+0.07}_{-0.07}$	-0.948
Si I	MB99	—	34	$1.83^{+0.10}_{-0.12}$	$-0.30^{+0.02}_{-0.03}$	-0.663
Si I	VALD	—	31	$1.68^{+0.29}_{-0.29}$	$-0.40^{+0.06}_{-0.05}$	-0.739
Si I	VALD	NLTE	21	$1.49^{+0.32}_{-0.37}$	$-0.41^{+0.09}_{-0.07}$	-0.835
Ti I	MB99	—	25	$1.58^{+0.24}_{-0.21}$	$-0.11^{+0.04}_{-0.04}$	-0.788
Ti I	VALD	—	34	$1.57^{+0.18}_{-0.15}$	$-0.34^{+0.04}_{-0.04}$	-0.937
Ti I	VALD	NLTE	32	$1.45^{+0.18}_{-0.15}$	$-0.22^{+0.04}_{-0.05}$	-0.907
<i>μ Leo</i>						
Fe I	MB99	—	67	$1.34^{+0.12}_{-0.12}$	$0.29^{+0.04}_{-0.04}$	-0.879
Fe I	VALD	—	85	$1.05^{+0.17}_{-0.17}$	$0.16^{+0.08}_{-0.07}$	-0.909
Fe I	VALD	NLTE	55	$1.04^{+0.22}_{-0.21}$	$0.14^{+0.10}_{-0.09}$	-0.903
Si I	MB99	—	38	$2.25^{+0.21}_{-0.20}$	$0.22^{+0.05}_{-0.05}$	-0.820
Si I	VALD	—	33	$1.67^{+0.46}_{-0.40}$	$0.21^{+0.07}_{-0.07}$	-0.834
Si I	VALD	NLTE	19	$1.52^{+0.54}_{-0.38}$	$0.21^{+0.07}_{-0.09}$	-0.871
Ti I	MB99	—	29	$2.11^{+0.40}_{-0.34}$	$0.26^{+0.06}_{-0.06}$	-0.834
Ti I	VALD	—	35	$1.81^{+0.35}_{-0.26}$	$0.10^{+0.07}_{-0.08}$	-0.921
Ti I	VALD	NLTE	30	$1.71^{+0.31}_{-0.24}$	$0.16^{+0.07}_{-0.08}$	-0.902

NOTE— The third column (NLTE) indicates whether the non-LTE correction was applied or not. The fourth column (N) indicates the number of lines used for estimating the microturbulence, ξ , and the abundance, $[X/H]$. The $[X/H]$ are scaled with respect to the solar abundance in Grevesse et al. (2007). The last column (r) indicates the correlation coefficient (see the definition in Paper I) between ξ and $[X/H]$.

rections for Fe I lines are mostly within 0.05 dex and have little impact on the ξ . In fact, the difference of 0.14 km s^{-1} with and without the non-LTE corrections can be explained by the difference in the lines used for the calculation; using the 47 lines to which we could apply the corrections leads to $\xi \sim 1.42 \text{ km s}^{-1}$ even if we do not apply the corrections. The non-LTE corrections are as large as 0.15 dex (or -0.15 dex) for some Si I and Ti I lines. In addition, there are weak correlations between the line strengths and the non-LTE correlations, leading to slightly lower ξ , though the impacts on (ξ , $[X/H]$) are not really significant (Figure 4). The same analysis can be done with the MB99 lines. However, the primary purpose of this part is to see the relative impact of the non-LTE corrections on the microturbulence, and

we examined the results with the non-LTE corrections only for the VALD3 line sets.

As the contours in Figure 4 suggest, the abundance we obtain depends on the microturbulence. If we fix ξ to the one obtained with Fe I lines, $[Si/H]$ and $[Ti/H]$ get higher than the ones obtained with the bootstrap analysis (Section 3.3). If we knew the true abundances, we would be able to determine the ξ that leads to accurate abundances. However, we cannot draw such a conclusion because previously reported values of $[Si/H]$ and $[Ti/H]$ have large scatters. Figure 5 compares our estimates with previous results for Arcturus (Thevenin 1998; Luck & Heiter 2005; Fulbright et al. 2007; Worley et al. 2009; Chou et al. 2010; Ramírez & Allende Prieto 2011; Britavskiy et al. 2012; Smith et al. 2013; Jofré et al. 2015) and μ Leo (McWilliam 1990; Thevenin 1998; Smith & Ruck 2000; Luck & Heiter 2007; Smith et al. 2013; Jofré et al. 2015). Here, we only refer to the reports in which the solar-abundance reference is apparent, and all the $[X/H]$ are scaled with respect to the solar compositions in Grevesse et al. (2007). Regardless of which line lists are used and which of the ξ in Table 4 are used, our estimates are within the scatters of literature values.

Takeda (1992) investigated the microturbulence of Arcturus and found that different groups of lines tend to give different ξ showing the correlation with the depth of line forming layers (also see Gray 1981, for an earlier report on the depth-dependent ξ of Arcturus). They found that the derived ξ values depend on the properties of the line sets, e.g., the EPs and the ionization stage of the lines included; ξ tends to be smaller with the lines formed in the inner atmosphere used in the analysis. Roughly speaking, the depth of a line forming region is well correlated with the line strength as expected, while the EP and some other parameters have additional effects (Gurtovenko & Sheminova 2015). As seen in Figure 3, the distributions of depths of the Fe I, Si I, and Ti I lines used for the analysis are similarly broad and uniform between the shallowest (0.03) and the deepest (0.35). At least, not all the Si I and Ti I lines are formed in layers higher than Fe I lines. There appears to be no simple reason to expect that both Si I and Ti I give ξ higher than Fe I. Moreover, while determining ξ accurately requires large numbers of lines (Mucciarelli 2011), the numbers of lines available for each group tend to be limited. The problem with the limited numbers of lines is particularly severe with infrared spectra; in our case, we can use less than 100 lines even for Fe I, which results in the significant statistical errors in ξ . The limited line number prevents us from more detailed discussions such as using a subset of lines, e.g., those with high or

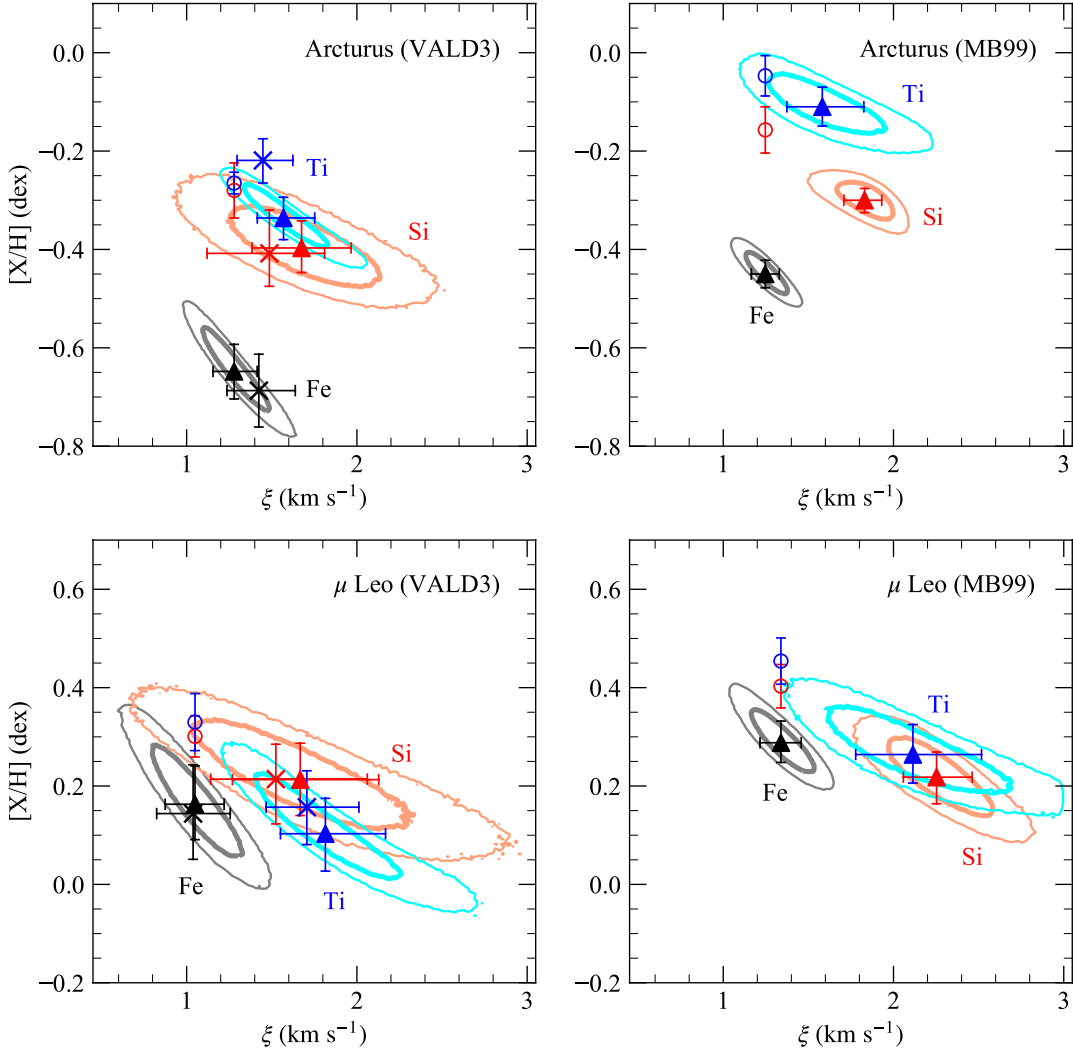


Figure 4. Solutions of the bootstrap method for measuring the abundance, $[X/H]$, and the microturbulence, ξ , for the three elements (Fe, Si, and Ti). Each of the four panels shows the results for a combination of the line list (VALD3 or MB99) and the object (Arcturus or μ Leo). The best estimates of $(\xi, [X/H])$ for individual atoms (listed in Table 4) are indicated by filled triangles, and the contours indicate the ranges around the best estimate encircling 68.26% (inner) or 95.44% (outer) of the bootstrap samples. The best estimates and contours are presented in different colors for different elements: Fe in black, Si in red, and Ti in blue. For the analysis with VALD, the results with the non-LTE corrections included (also listed in Table 4) are indicated by ‘ \times ’ markers. Open circles for Si and Ti indicate the best estimates with ξ fixed to that obtained for Fe (listed in Table 5).

low EPs only, for the ξ estimation (see the simulation described in Appendix B concerning the number of lines required for the bootstrap analysis). Moreover, we did not apply the method for determining ξ with the line of the other elements (i.e., Mg I, Ca I, and Ni I) because each of these elements give less than ~ 10 lines.

Considering the above situation, we fix ξ to the one determined for Fe I and use it for other elements, which is a standard procedure of the classical analysis involved with the depth-independent ξ . Moreover, the abundances measured with the same approach should be used

together in discussions about the features on $[\text{Fe}/\text{H}]$ – $[\text{X}/\text{Fe}]$ diagrams, and it is more common to fix ξ to the one estimated with Fe I lines. The depth dependency of ξ is an important and interesting issue. Still, the primary purpose of this paper is the line identification, neither determining the depth-dependent ξ nor precise calibration of the oscillator strengths of individual lines.

3.3. Abundances of the six elements and iron

In the following analysis, we used the ξ that we obtained with Fe I lines without the non-LTE effect corrected to measure the abundances of the six elements

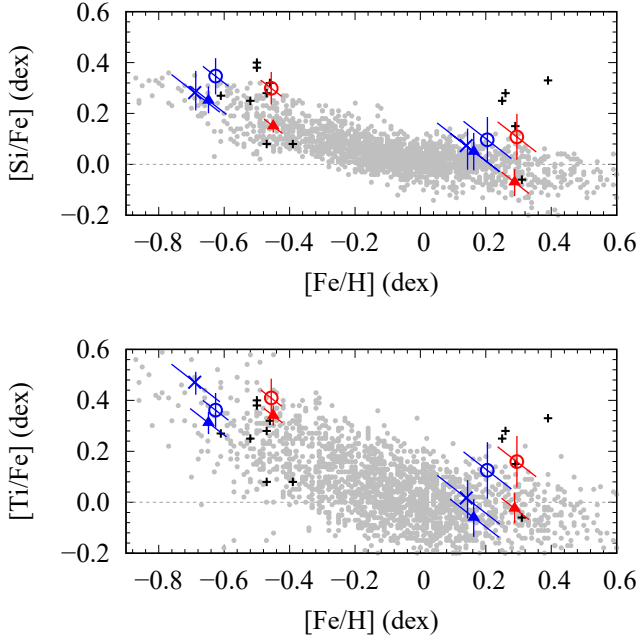


Figure 5. Comparison of the abundances of Arcturus and μ Leo derived by using different methods and line lists on the $[X/Fe]$ - $[Fe/H]$ diagrams. The results based on the VALD3 lines are illustrated in blue, and those based on the MB99 lines in red. The two objects have distinctly different metallicities (Arcturus being metal poor), and the same markers are used for both of them within each panel. Filled triangles indicate the results with the microturbulences estimated for individual elements with all the available lines used, while the VALD3 lines for which the non-LTE effects were taken into account were used for the results indicated by ‘ \times ’ marker (Table 4). The microturbulences were fixed to those obtained with Fe I lines to give the results indicated by open circles (Table 5). Small ‘+’ markers indicate the literature results for the two objects (references given in text). The gray small dots indicate the abundances of red giants with the APOGEE and Kepler data obtained by [Hawkins et al. \(2016\)](#). Two error bars are given to each point for representing Δ_{tot} in $[Fe/H]$ (sloped) and Δ_{tot} in $[X/H]$ (vertical). The total error, Δ_{tot} (Equation 4), is explained in Section 3.3.

(Mg I, Si I, Ca I, Ti I, Cr I, and Ni I) as well as Fe I. For each combination of the object (Arcturus and μ Leo) and the line list (VALD3 or MB99), we made the MPFIT measurements with the ξ obtained for Fe I (Table 4). Tables 1 and 2 list thus obtained abundances with individual lines selected for each combination. The flags of (w) or (b) are given to the lines that were not selected because they are weak or blended (according to β_1 and β_2). The abundances of the lines with the (s) flag were not measured because they are selected but deeper than 0.35 in depth, while the flag of (*) is given to Si I 10407.037 in the case of μ Leo (see Section 3.1).

Table 5 lists the number, N , of the lines with which we measured $[X/H]$ together with the standard deviation (SD) and the interquartile range (IQR) of the N values for each combination of line list and object. Figure 6 shows box plots of derived abundances. We took the median of the N values as the best estimate of the abundance. To estimate its error, we took a bootstrap approach; we generated 10000 bootstrapping samples of the N values and calculated the SD of the 10000 median values from individual bootstrapping samples. This SD, Δ_{med} , is considered as the statistical error of the final $[X/H]$. We obtained these estimates for seven elements, including Fe I (Table 5). It is worthwhile to note that both SDs and IQRs are large for many combinations of line list and object, $\text{IQR} \gtrsim 0.15$ dex for Arcturus and $\text{IQR} \gtrsim 0.25$ dex for μ Leo. Moreover, the ratio of IQR to SD is expected to be 1.35 for the Gaussian distribution, but the ratios in Table 5 are not normal for some combinations. These suggest that the $\log gf$ values in the current lists are not sufficiently precise, and the errors for some lines are particularly large, leading to outliers. We will come back to this point in Section 3.4.

We also estimated how much the uncertainties in the stellar parameters (T_{eff} , $\log g$, $[M/H]$, and ξ) affect the estimates of the abundances. We adopt the error in each parameter from [Heiter et al. \(2015\)](#) as the offset, σ_p , given in Table 6. To evaluate the effects of changing these parameters, we added positive and negative offsets to each parameter of the atmosphere models one by one. For each offset, we ran MPFIT and measured how much the abundance of each line is altered by the offset. We then took the median of the relative changes as the impact of each parameter on the abundance, Δ_p , where p is one of the stellar parameters. If the sizes of the positive and negative offsets are different from each other, we consider the root-mean-squares for σ_p and/or Δ_p ; e.g., σ_ξ tends to be asymmetric, and σ_ξ and Δ_ξ in Table 6 are the root-mean-squares. Figure 7 shows the Δ_p corresponding to the positive σ_p offsets of each parameter for Arcturus with VALD3 used for the measurements. The size of Δ_p varies with the element, and the sign of Δ_p also differs from one element to another in the case of $\Delta_{T_{\text{eff}}}$. The trends of Δ_p seen in Figure 7 are similar in the other combinations of line list and object. The trends for individual elements are described in Appendix A.

The trend of $\Delta_{\log g}$ is noteworthy. This dependency on $\log g$ is very small for Ca I, Ti I, and Cr I, in particular, while it is non-zero for other elements. For the three elements, the first ionization stage dominates in the entire range of line-formation layers relevant to this study, and the line absorption coefficient (l_ν) is expected

Table 5. Abundances Obtained Based on the Two Line Lists

Atom	List	N	SD (dex)	IQR (dex)	$[X/H]$ (dex)
<i>Arcturus</i>					
Mg I	VALD3	10	0.235	0.264	-0.176 ± 0.074
Mg I	MB99	6	0.100	0.056	-0.173 ± 0.042
Si I	VALD3	31	0.220	0.298	-0.280 ± 0.056
Si I	MB99	34	0.179	0.295	-0.157 ± 0.047
Ca I	VALD3	11	0.177	0.149	-0.370 ± 0.040
Ca I	MB99	7	0.378	0.120	-0.218 ± 0.116
Ti I	VALD3	34	0.120	0.107	-0.265 ± 0.022
Ti I	MB99	28	0.309	0.206	-0.047 ± 0.041
Cr I	VALD3	18	0.262	0.161	-0.608 ± 0.032
Cr I	MB99	14	0.094	0.104	-0.443 ± 0.030
Fe I	VALD3	66	0.196	0.174	-0.626 ± 0.018
Fe I	MB99	53	0.100	0.120	-0.456 ± 0.018
Ni I	VALD3	9	0.151	0.232	-0.581 ± 0.070
Ni I	MB99	3	0.125	0.143	-0.363 ± 0.119
<i>μ Leo</i>					
Mg I	VALD3	9	0.426	0.256	0.307 ± 0.122
Mg I	MB99	7	0.384	0.105	0.166 ± 0.115
Si I	VALD3	34	0.293	0.384	0.301 ± 0.042
Si I	MB99	36	0.313	0.284	0.403 ± 0.044
Ca I	VALD3	13	0.278	0.216	0.277 ± 0.054
Ca I	MB99	20	0.239	0.213	0.341 ± 0.034
Ti I	VALD3	36	0.433	0.341	0.330 ± 0.058
Ti I	MB99	31	0.243	0.332	0.454 ± 0.047
Cr I	VALD3	25	0.234	0.316	0.248 ± 0.052
Cr I	MB99	21	0.203	0.236	0.361 ± 0.054
Fe I	VALD3	84	0.309	0.353	0.205 ± 0.033
Fe I	MB99	68	0.167	0.247	0.295 ± 0.027
Ni I	VALD3	11	0.405	0.602	0.383 ± 0.182
Ni I	MB99	7	0.391	0.774	0.067 ± 0.279

NOTE— For each combination of line list and object, N lines were used for the abundance measurements with the microturbulence, ξ , fixed. The abundances from N individual lines, showing the standard deviation (SD) and the interquartile range (IQR) in the table, were combined to obtain the final abundance, $[X/H]$, and its error.

to be proportional to the electron pressure. The continuum absorption coefficient (κ_ν) is also proportional to the electron pressure around T_{eff} of our targets because it is dominated by the negative hydrogen (H^-). Then, the line depths ($\approx l_\nu/\kappa_\nu$) are expected to be insensitive to the electron pressure and to the surface gravity as suggested by the small $\Delta_{\log g}$ (Gray 2005; see, also, Jian

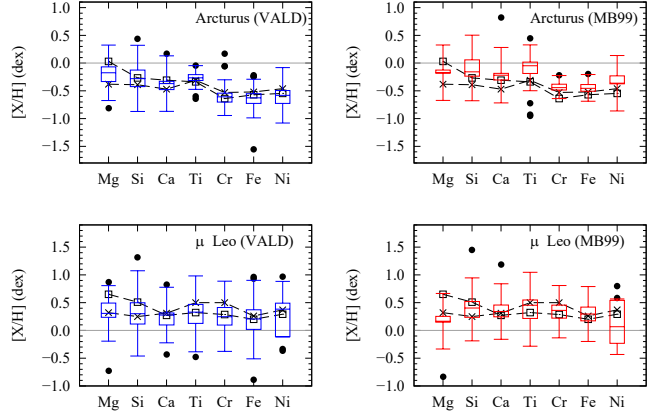


Figure 6. Box plots of abundances derived with individual lines for each combination of object and line list. The lower, middle, and upper lines of a box indicate the quartiles (the 25 percentile, the median, and the 75 percentile). The upper and lower extremes of the whiskers indicate the thresholds of the outlier detection, and black filled circles indicate the outliers (discussed in the text). Crosses and squares indicate the abundance ratios reported by Smith et al. (2013) and Jofré et al. (Jofré et al. 2014 for Fe and Jofré et al. 2015 for the other elements), respectively.

et al. 2020). In case of other elements, in contrast, weak lines are formed in more ionized layers (the ionization fraction ~ 60 to almost 100%), while the ionization fraction drops significantly, down to a few percent in some cases, in the forming layers of strong lines. This results in the non-zero dependency on $\log g$. This explains the $\Delta_{\log g}$ presented in Figure 7 well.

Combining the Δ_p values with the statistical error (Δ_{med}) estimated with the bootstrap analysis, we calculated the total error, Δ_{tot} , by

$$\Delta_{\text{tot}}^2 = \Delta_{T_{\text{eff}}}^2 + \Delta_{\log g}^2 + \Delta_{[M/H]}^2 + \Delta_{\xi}^2 + \Delta_{\text{med}}^2 \quad (4)$$

where we ignored the covariant terms as we did in Paper I. The stellar parameters used for Figure 2 of Paper I show no clear correlation between any two of them (T_{eff} , $\log g$, $[M/H]$, and ξ). The results are given in Table 6.

3.4. Comparison with previous results

Figure 8 compares our two estimates of $[X/H]$ based on the VALD3 and MB99 for each element with those reported by Smith et al. (2013) and Jofré et al. (2014; 2015). The former study used H -band spectra, whereas the latter used optical spectra. The total errors, Δ_{tot} in Table 6, are used for the error bars for our results. The errors we use for the results in Smith et al. (2013) and Jofré et al. also combine statistical errors and systematic errors. The definition of the statistical errors given in their works is, however, different from that of

Table 6. Effects of Stellar Parameters and Abundance Errors

Δ_p	σ_p	Mg I	Si I	Ca I	Ti I	Cr I	Fe I	Ni I
<i>Arcturus with VALD3</i>								
$\Delta_{T_{\text{eff}}}$	± 35 K	± 0.001	∓ 0.029	± 0.015	± 0.060	± 0.038	± 0.003	∓ 0.011
$\Delta_{\log g}$	± 0.06 dex	± 0.001	± 0.014	∓ 0.000	± 0.002	± 0.001	± 0.011	± 0.015
$\Delta_{[\text{M}/\text{H}]}$	± 0.08 dex	± 0.021	± 0.022	∓ 0.003	∓ 0.003	∓ 0.001	± 0.014	± 0.019
Δ_{ξ}	± 0.08 km s $^{-1}$	∓ 0.005	∓ 0.020	∓ 0.009	∓ 0.022	∓ 0.017	∓ 0.030	∓ 0.019
Δ_{med}	—	0.074	0.056	0.040	0.022	0.032	0.018	0.070
Δ_{tot}	—	0.077	0.071	0.044	0.068	0.052	0.039	0.077
<i>Arcturus with MB99</i>								
$\Delta_{T_{\text{eff}}}$	± 35 K	± 0.000	∓ 0.030	± 0.015	± 0.062	± 0.037	± 0.008	∓ 0.010
$\Delta_{\log g}$	± 0.06 dex	± 0.003	± 0.015	∓ 0.001	± 0.003	± 0.001	± 0.011	± 0.017
$\Delta_{[\text{M}/\text{H}]}$	± 0.08 dex	± 0.019	± 0.023	∓ 0.003	∓ 0.003	∓ 0.001	± 0.014	± 0.018
Δ_{ξ}	± 0.13 km s $^{-1}$	∓ 0.012	∓ 0.016	∓ 0.005	∓ 0.015	∓ 0.011	∓ 0.019	∓ 0.031
Δ_{med}	—	0.042	0.047	0.116	0.041	0.030	0.018	0.119
Δ_{tot}	—	0.048	0.064	0.117	0.076	0.049	0.032	0.126
<i>μ Leo with VALD3</i>								
$\Delta_{T_{\text{eff}}}$	± 60 K	∓ 0.008	∓ 0.059	± 0.025	± 0.082	± 0.051	∓ 0.009	∓ 0.026
$\Delta_{\log g}$	± 0.09 dex	± 0.001	± 0.021	∓ 0.005	± 0.003	± 0.004	± 0.016	± 0.022
$\Delta_{[\text{M}/\text{H}]}$	± 0.15 dex	± 0.033	± 0.043	∓ 0.006	± 0.001	± 0.008	± 0.032	± 0.043
Δ_{ξ}	± 0.12 km s $^{-1}$	∓ 0.008	∓ 0.026	∓ 0.023	∓ 0.048	∓ 0.061	∓ 0.053	∓ 0.050
Δ_{med}	—	0.122	0.042	0.054	0.058	0.052	0.033	0.182
Δ_{tot}	—	0.127	0.090	0.064	0.111	0.095	0.073	0.197
<i>μ Leo with MB99</i>								
$\Delta_{T_{\text{eff}}}$	± 60 K	∓ 0.007	∓ 0.060	± 0.025	± 0.085	± 0.051	∓ 0.008	∓ 0.022
$\Delta_{\log g}$	± 0.09 dex	± 0.002	± 0.025	∓ 0.003	± 0.004	± 0.004	± 0.020	± 0.026
$\Delta_{[\text{M}/\text{H}]}$	± 0.15 dex	± 0.041	± 0.039	± 0.001	± 0.000	± 0.008	± 0.031	± 0.041
Δ_{ξ}	± 0.18 km s $^{-1}$	∓ 0.020	∓ 0.021	∓ 0.006	∓ 0.029	∓ 0.031	∓ 0.036	∓ 0.004
Δ_{med}	—	0.115	0.044	0.034	0.047	0.054	0.027	0.279
Δ_{tot}	—	0.124	0.090	0.043	0.101	0.081	0.059	0.284

NOTE— In the first four lines for each combination of the object and the line list, σ_p indicates the error, in the parameter p , that was used for estimating Δ_p , i.e., the effect of p on the abundance $[\text{X}/\text{H}]$. In the last two lines, Δ_{med} indicates the error in Table 5, and Δ_{tot} is the total error estimated with Equation 4.

ours. Their statistical errors are the SDs of abundances from individual lines. Their SDs tend to be significantly smaller than the SDs in Table 5. This can be ascribed to the difference in the line selection and the quality of $\log gf$ values; we have not selected the lines on the basis of the accuracy of $\log gf$. The astrophysical calibration of the $\log gf$ values remains to be done, desirably, for red giants with each of the abundance-analysis tools. As for the systematic errors, all of these works estimated the effects of stellar parameters and, for all the points in Figure 8, we combined Δ_p , in our notation, of the four parameters (T_{eff} , $\log g$, $[\text{M}/\text{H}]$, and ξ) by the square root of sum of squares without the covariant terms taken into account.

Quantitative analysis on the accuracy of $\log gf$, or their re-calibration, is outside the scope of this paper. Still, we can identify the lines that seem to have $\log gf$ with larger errors than other lines, and give caution flags to them. Si I, Ti I, Cr I, and Fe I have more than 20 lines selected, and we identified outliers among their lines by considering the IQR rule. Let q_{25} , q_{50} , and q_{75} denote the quartiles of the $[\text{X}/\text{H}]$; q_{50} corresponds to the median, and the IQR is given by $q_{75} - q_{25}$. We here use the $1.5 \times \text{IQR}$ rule for the outlier detection, i.e., the derived abundance of a line is judged as an outlier if it is smaller than $q_{25} - 1.5 \text{ IQR}$ or larger than $q_{75} + 1.5 \text{ IQR}$. In contrast, the numbers of lines are small for Mg I, Ca I, and Ni I, and we use $q_{50} \pm 0.5$ dex as the thresholds of out-

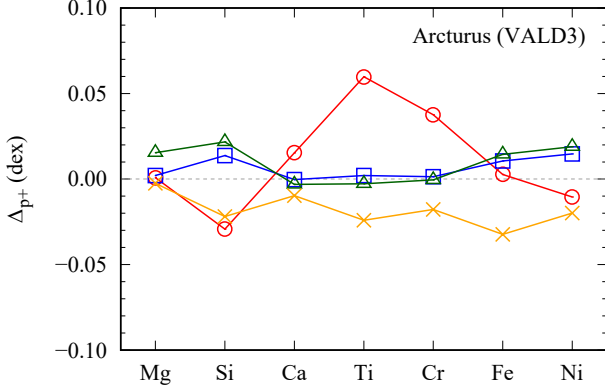


Figure 7. The effects of changing stellar parameters on the abundance of Arcturus measured with the VALD3 lines. The effects were measured by changing each parameter at a time, and Δ_{p+} shown in this plot (also see Table 6) indicates how much $[X/H]$ changes with the positive offset in the parameter p , $+35$ K in T_{eff} (red circles), $+0.06$ dex in $\log g$ (green triangles), $+0.08$ dex in $[M/H]$ (blue squares), and $+0.14$ km s $^{-1}$ in ξ (orange crosses).

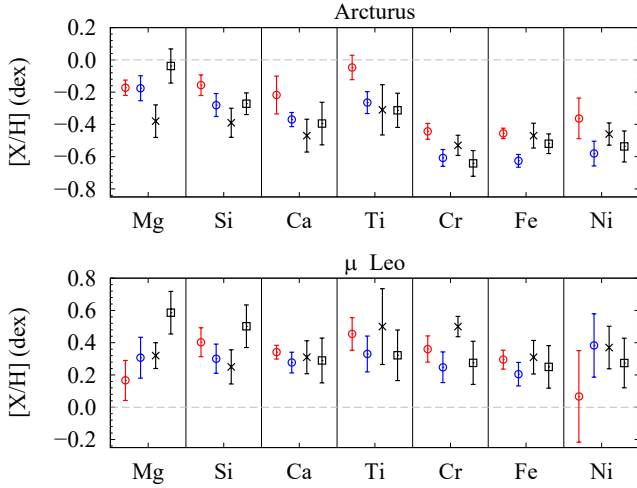


Figure 8. The final abundances of Arcturus and μ Leo based on VALD3 (blue) and MB99 (red). Their statistical errors in Table 5 and the total errors in Table 6 are drawn in the bright colors and pale colors. Black crosses and squares indicate the values reported by Smith et al. (2013) and Jofré et al. (Jofré et al. 2014 for Fe; Jofré et al. 2015 for the other elements), respectively. The definitions of the error bars are given in the text.

liers. For each line in a given line list, the flag is given as follows. We combine the number of objects for which the abundance was measured (N_{obj}) and the number of measurements found to be outliers (N_{out}) and give the flag, $N_{\text{out}}/N_{\text{obj}}$. If the line was not used for the abundance measurement, with the flags such as (w) and (s),

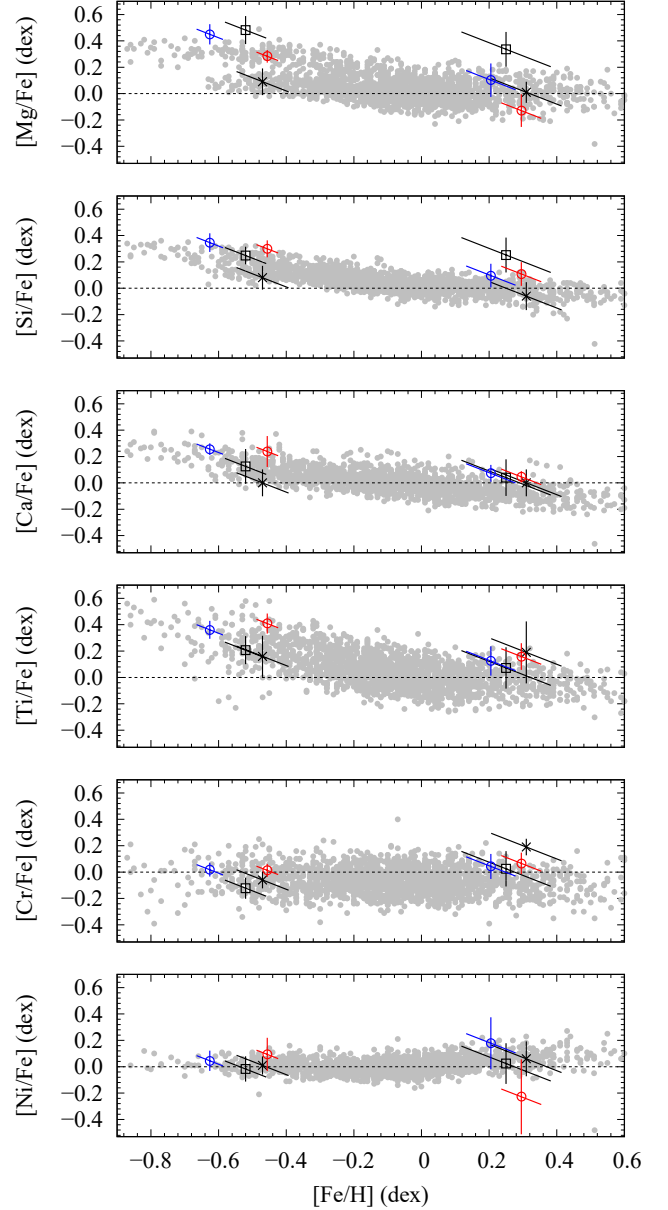


Figure 9. Abundances of Arcturus (metal-poor) and μ Leo (metal-rich) derived with different line lists (VALD3 presented in blue and MB99 in red). The microturbulences were fixed to those obtained with Fe I lines for deriving the abundances of all the elements, including Fe. Black crosses and squares indicate the values reported by Smith et al. (2013) and Jofré et al. (Jofré et al. 2014 for Fe; Jofré et al. 2015 for the other elements), respectively. For each point of $([Fe/H], [X/H])$, two error bars are given to represent the effect of $\Delta_{\text{tot}}([Fe/H])$ (sloped) and that of $\Delta_{\text{tot}}([X/H])$ (vertical). The gray small dots indicate the abundances of red giants with the APOGEE and Kepler data obtained by Hawkins et al. (2016).

for an object, it is not included in N_{obj} and the outlier detection was not performed. Thus-determined flags are given in Table 1 and 2. The flag of ‘2/2’ suggests that the abundances derived for both objects are judged as outliers, indicating that the $\log gf$ of such a line has a large error. For example, Ca I 12816.05 was judged as an outlier in all cases, the $\log gf$ of this line in both VALD3 and MB99 are considered to be rather inaccurate. We gave non-zero flags (i.e., $N_{\text{out}} \neq 0$) to 21 lines in VALD3 and 11 lines in MB99. We added the colon mark (:) to the abundances judged as outliers in Table 1 and 2.

Concerning the systematics of the abundance scales based on the two line lists, the $[X/H]$ based on MB99 are systematically higher than the counterparts with VALD3 by 0.1–0.2 dex for both objects except Mg I and Ni I for which the numbers of available lines are small. Roughly speaking, the best estimates in Figure 8 agree with each other allowing for scatters of ~ 0.2 dex. Figure 9 compares our estimates with the abundance trends on the $[X/Fe]$ – $[Fe/H]$ diagrams reported by Hawkins et al. (2016), who measured the abundances of disk stars. VALD3 and MB99 place Arcturus and μ Leo at slightly different positions, but the results are still consistent with the trends of disk stars as expected (e.g., Smith et al. 2013). While the difference of the metallicity scales is not negligible, $\gtrsim 0.1$ dex different in $[Fe/H]$, we cannot select one of them based on the comparison in Figure 9.

4. CONCLUDING REMARKS

We identified absorption lines of six elements (Mg I, Si I, Ca I, Ti I, Cr I, and Ni I) that appear in the $z'YJ$ -band spectra of red giants and are relatively isolated. From the large compilations of VALD3 and MB99, ~ 10 (for Ni I and Mg I) to over 30 (for Si I and Ti I) lines were selected for each element. Some detailed discussions on the selected lines for each element are given in Appendix A. These lines combined with >50 Fe I lines reported in Paper I are useful for the abundance analysis of red giants with $z'YJ$ -band spectra, which will be particularly important for obtaining the precise metallicities of stars obscured by severe interstellar extinction that hampers optical spectroscopy.

With the abundance analysis making use of classical 1D LTE atmospheric models (ATLAS9 in our case), the microturbulence, ξ , is a crucial parameter required for

obtaining accurate results. We measured ξ that gives $[X/H]$ independent of line strength for each of Si I and Ti I. They are slightly higher than those determined for Fe I, and the differences in ξ are large enough to give significant impacts on the abundances, 0.1–0.2 dex. Therefore, unless it turns out that a common ξ can be used for every element, finding a good ξ for each element will be an essential step in order to improve the accuracy of the abundance measurements in the future. Another vital error source is the systematics of the oscillator strengths given in the two line lists. VALD3 and MB99 tend to give slightly different abundances, 0.1–0.2 dex higher if the MB99 is used. The scatters of the abundances in previous studies prevent us from judging which of VALD3 and MB99 gives more accurate results.

ACKNOWLEDGMENTS

We are grateful to the staff of Koyama Astronomical Observatory for their support during our observation. This study is supported by KAKENHI (Grants-in-Aid, Nos. 26287028 and 18H01248) from the Japan Society for the Promotion of Science (JSPS). The WINERED was developed by the University of Tokyo and the Laboratory of Infrared High-resolution spectroscopy (LiH), Kyoto Sangyo University under the financial supports of JSPS KAKENHI (Nos. 16684001, 20340042, 21840052) and the Supported Programs for the Strategic Research Foundation at Private Universities (Nos S0801061 and S1411028) from the Ministry of Education, Culture, Sports, Science and Technology (MEXT) of Japan. This study has made use of the SIMBAD database, operated at CDS, Strasbourg, France and also the VALD database, operated at Uppsala University, the Institute of Astronomy RAS in Moscow, and the University of Vienna. K.F. is supported by a JSPS Grant-in-Aid for Research Activity Start-up (No. 16H07323). N.K. is supported by JSPS-DST under the Japan-India Science Cooperative Programs during 2013-2015 and 2016-2018.

Software: WINERED pipeline (S. Hamano et al. 2021, in preparation), IRAF (Tody 1986, 1993), PyRAF (Science Software Branch at STScI, 2012), SPTOOL (Y. Takeda, private communication).

APPENDIX

A. LINES SELECTED FOR INDIVIDUAL ELEMENTS

1. Mg I (Magnesium, $Z = 12$)— 12 and 8 Mg I lines from VALD3 and MB99, respectively, are included

in our line lists. Mg I 11820.982 in VALD3 was listed up with the synthetic spectra but not included because its absorption was not confirmed in the observed spectra. All the 8 lines from MB99

are also included in the VALD3 list. The EPs of 11 lines are high, > 5.9 eV, but Mg I 11828 has a low EP, ~ 4.35 eV though it is too strong to be used for our abundance measurements. The abundances estimated with individual lines tend to show a large scatter, but the median values are consistent with the literature values within the errors. Errors in the stellar parameters have relatively small impacts on the measurements of $[\text{Mg}/\text{H}]$.

2. Si I (Silicon, $Z = 14$)— 56 Si I lines are included in our lists in total, 50 lines from VALD3 and 49 lines from MB99 (43 lines being selected from both). All these lines have relatively high EPs, $\gtrsim 5$ eV. Their depths cover a wide range from shallow to deep, and several lines are too strong to be used for the abundance measurements. The abundances with individual lines show large scatters, but the resultant abundances and the errors are comparable with those in the literature. $[\text{Si}/\text{H}]$ obtained with VALD3 are slightly lower, by ~ 0.1 dex, than those obtained with MB99.
3. Ca I (Calcium, $Z = 20$)— 15 lines are selected from VALD3, while 17 lines are selected from MB99. There are 10 lines in common, of which Ca I 10343 in both lists is too strong to be used for the abundance measurements. More than half of the MB99 lines are too weak in Arcturus but are measurable in μ Leo. Ca I 12816 has highly inaccurate $\log gf$ values, by more than 0.5 dex, in the two lists, but other lines lead to reasonable estimates of $[\text{Ca}/\text{H}]$. The abundances estimated with VALD3 are lower than those with MB99 by 0.1–0.15 dex.
4. Ti I (Titanium, $Z = 22$)— In total, 54 Ti I lines (50 lines from VALD3 and 34 from MB99) are included in our lists in total. Most of them have EPs lower than 2 eV except a few with EP ~ 4 eV. The strengths range from weak to very strong over the limit, 0.35 in depth, beyond which we did not perform the abundance measurements. The dependency of derived $[\text{Ti}/\text{H}]$ on T_{eff} and also on ξ is strong. The abundances estimated with VALD3 are lower than those with MB99 by 0.1–0.2 dex.
5. Cr I (Chromium, $Z = 24$)— 25 and 21 Cr I lines are selected from VALD3 and MB99, respectively, with 19 lines in common and 27 lines in total. There are not very strong lines, i.e., no Cr I line is deeper than 0.35 in either Arcturus or μ Leo, while several lines are too weak in Arcturus. The dependency of derived $[\text{Cr}/\text{H}]$ on T_{eff} is relatively

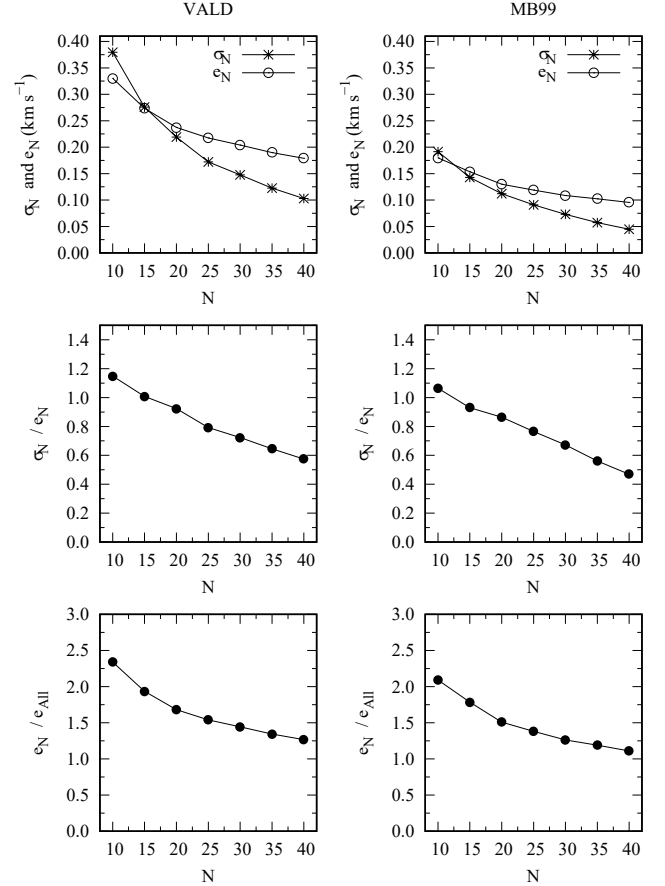


Figure 10. The simulation results on the bootstrap analysis with different numbers, N , of lines available. The parameters are described in the text. Here presented is the case of Arcturus ($e_{\text{All}} = 0.14 \text{ km s}^{-1}$ for VALD3, 0.09 km s^{-1} for MB99), and the left three panels plots the results with VALD3 and the right panels those with MB99.

strong. The abundances estimated with VALD3 are lower than those with MB99 by 0.1–0.15 dex.

6. Ni I (Nickel, $Z = 28$)— 15 Ni I lines (13 and 7 from VALD3 and MB99, respectively) are included in our line lists. No line is stronger than the limit of 0.35 in depth, but a few lines are too weak in Arcturus. The line sets used for the combinations of line list and object tend to be different. The abundances from individual lines show large scatters, especially for μ Leo, leading to the large errors in the final $[\text{Ni}/\text{H}]$, 0.1–0.3 dex, combined with the small line numbers.

B. SIMULATIONS OF BOOTSTRAP

We performed a simulation for investigating how many lines are required to derive the microturbulence, ξ , and abundance, $[\text{X}/\text{H}]$, simultaneously with the bootstrap

method. For this purpose, we used Fe I lines in Table 1 and 2, but excluded those with flags such as (s) and (w) in either of Arcturus or μ Leo. We found 60 VALD3 lines and 50 MB99 lines to use, and we repeat the following analysis for the four combinations of object (Arcturus or μ Leo) and line list (VALD3 or MB99). Let the set A indicate this starting line set (the number of lines being $N_{\text{All}} = 60$ for VALD3 and 50 for MB99). We first ran the bootstrap analysis for this set A , and compare this result, $\xi_{\text{All}} \pm e_{\text{All}}$, with the results with fewer lines as follows. As simulation sets of fewer lines, we repeated the random selection of N lines among those in the set A without duplication 1000 times for each N (N takes 10, 15, 20, \dots , 40). Each set of N lines gives an estimate of $\xi(j)$ together with the 1σ error range, $[\xi(j) - e_- : \xi(j) + e_+]$, where j varies from 1 to 1000. The error in $\xi(j)$ is given by $e(j) = \sqrt{(e_{\xi_-}^2 + e_{\xi_+}^2)/2}$. We thus obtained 1000 $e(j)$ values and calculated their

mean as the measure of the typical error (denoted as e_N) obtained with N lines. In addition, the standard deviation of the 1000 $\xi(j)$, denoted as σ_N , indicates how much the selection of N lines could affect the resultant microturbulence. Figure 10 shows these results for Arcturus. Both e_N and σ_N increase with decreasing N , as expected; the determination of ξ (and $[X/H]$) suffers from larger uncertainties if fewer lines are available. When the number of lines gets as small as 15–20, the statistical uncertainty (e_N) becomes 1.5–2 times as large as e_{All} . In addition, the effect of the line selection (σ_N) becomes as large as the statistical uncertainty, which means that the ξ we get is significantly affected by the systematic error caused by which lines are actually available and also by the precision of oscillator strengths of the particular line set. We therefore suggest that the bootstrap method of determining ξ and $[X/H]$ together requires ~ 20 lines at least, but this limit depends on the precision of $\log gf$.

REFERENCES

- Adibekyan, V., Figueira, P., Santos, N. C., et al. 2015, *A&A*, 583, A94
- Amarsi, A. M., Lind, K., Asplund, M., et al. 2016, *MNRAS*, 463, 1518
- Anders, E., & Grevesse, N. 1989, *GeoCoA*, 53, 197
- Andreasen, D. T., Sousa, S. G., Delgado Mena, E., et al. 2016, *A&A*, 585, A143
- Asplund, M. 2000, *A&A*, 359, 755
- Bergemann, M., Kudritzki, R.-P., Plez, B., et al. 2012, *ApJ*, 751, 156
- Bergemann, M., Kudritzki, R.-P., Würl, M., et al. 2013, *ApJ*, 764, 115
- Blackwell, D. E., & Willis, R. B. 1977, *MNRAS*, 180, 169
- Britavskiy, N. E., Andrievsky, S. M., Tsymbal, V. V., et al. 2012, *A&A*, 542, A104
- Chou, M.-Y., Cunha, K., Majewski, S. R., et al. 2010, *ApJ*, 708, 1290
- de Jager, C., Mulder, P. S., & Kondo, Y. 1984, *A&A*, 141, 304
- Dobrovolskas, V., Kučinskas, A., Steffen, M., et al. 2013, *A&A*, 559, A102
- Feltzing, S., & Chiba, M. 2013, *NewAR*, 57, 80
- Freeman, K., & Bland-Hawthorn, J. 2002, *ARA&A*, 40, 487
- Fulbright, J. P., McWilliam, A., & Rich, R. M. 2007, *ApJ*, 661, 1152
- Gratton, R., Bragaglia, A., Carretta, E., & Tosi, M. 2006, *ApJ*, 642, 462
- Gray, D. F. 1981, *ApJ*, 245, 992
- Gray, D. F. 2005, *The Observation and Analysis of Stellar Photospheres*
- Grevesse, N., Asplund, M., & Sauval, A. J. 2007, *SSRv*, 130, 105
- Gurtovenko, E. A. & Sheminova, V. A. 2015, *arXiv:1505.00975*
- Hawkins, K., Masseron, T., Jofré, P., et al. 2016, *A&A*, 594, A43
- Heiter, U., Jofré, P., Gustafsson, B., et al. 2015, *A&A*, 582, A49
- Ikeda, Y., Kobayashi, N., Kondo, S., et al. 2016, *Proc. SPIE*, 9908, 99085Z
- Jian, M., Taniguchi, D., Matsunaga, N., et al. 2020, *MNRAS*, 494, 1724
- Jofré, P., Heiter, U., Soubiran, C., et al. 2014, *A&A*, 564, A133
- Jofré, P., Heiter, U., Soubiran, C., et al. 2015, *A&A*, 582, A81
- Jofré, P., Heiter, U., & Soubiran, C. 2019, *ARA&A*, 57, 571
- Kondo, S., Fukue, K., Matsunaga, N., et al. 2019, *ApJ*, 875, 129
- Kurucz, R. L. 1993, *Kurucz CD-ROM*, Cambridge, MA: Smithsonian Astrophysical Observatory, —c1993, December 4, 1993,
- Luck, R. E., & Heiter, U. 2005, *AJ*, 129, 1063
- Luck, R. E. & Heiter, U. 2007, *AJ*, 133, 2464
- Magain, P. 1984, *A&A*, 134, 189
- Matsunaga, N., Taniguchi, D., Jian, M., et al. 2020, *ApJS*, 246, 10

- McWilliam, A. 1990, *ApJS*, 74, 1075
- Meléndez, J., & Barbuy, B. 1999, *ApJS*, 124, 527
- Mucciarelli, A. 2011, *A&A*, 528, A44
- Niemczura, E., Smalley, B., & Pych, W. 2014, Determination of Atmospheric Parameters of B-, A-, F- and G-Type Stars Lectures from the School of Spectroscopic Data Analyses, edited by E. Niemczura et al. ISBN 978-3-319-06955-5. Berlin: Springer-Verlag, 2014
- Ramírez, I., & Allende Prieto, C. 2011, *ApJ*, 743, 135
- Ryabchikova, T., et al. 2015, *Phys. Scripta*, 90, 054005
- Sameshima, H., Matsunaga, N., Kobayashi, N., et al. 2018, *PASP*, 130, 074502
- Sheminova, V. A. 2015, *Kinematics and Physics of Celestial Bodies*, 31, 172
- Smith, G., & Ruck, M. J. 2000, *A&A*, 356, 570
- Smith, V. V., Cunha, K., Shetrone, M. D., et al. 2013, *ApJ*, 765, 16
- Takeda, Y. 1992, *A&A*, 253, 487
- Takeda, Y. 1995, *PASJ*, 47, 287
- Taniguchi, D., et al. 2018, *MNRAS*, 473, 4993
- Thevenin, F. 1998, *VizieR Online Data Catalog*, III/193
- Tody, D. 1986, *Proc. SPIE*, 627, 733
- Tody, D. 1993, *Astronomical Data Analysis Software and Systems II*, 52, 173
- Worley, C. C., Cottrell, P. L., Freeman, K. C., & Wylie-de Boer, E. C. 2009, *MNRAS*, 400, 1039

Table 1. Lines Selected from VALD3 and Abundances

λ_{air} (Å)	Atom	EP (eV)	$\log gf$ (dex)	Arcturus (dex)	μ Leo (dex)	flag
9117.1309	Fe I	2.8581	-3.454	-0.37	0.36	0/2
9118.8806	Fe I	2.8316	-2.115	(s)	(s)	0/0
9123.2029	Ti I	3.1129	-0.619	-0.38	-1.84:	1/2
9146.1275	Fe I	2.5881	-2.804	-0.61	-0.35	0/2
9210.0240	Fe I	2.8450	-2.404	-0.65	(s)	0/1
9602.1301	Fe I	5.0117	-1.744	(w)	0.11	0/1
9638.3043	Ti I	0.8484	-0.612	(s)	(s)	0/0
9647.3700	Ti I	0.8181	-1.434	(s)	(s)	0/0
9653.1147	Fe I	4.7331	-0.684	-0.61	0.31	0/2
9657.2326	Fe I	5.0856	-0.780	-0.65	-0.20	0/2
9667.2850	Cr I	2.5438	-2.510	-0.05	0.81:	1/2
9670.5390	Cr I	2.5443	-1.790	0.17	0.53:	1/2
9675.5433	Ti I	0.8360	-0.804	(s)	(b)	0/0
9688.8729	Ti I	0.8129	-1.610	(s)	(b)	0/0
9705.6640	Ti I	0.8259	-1.009	(s)	(s)	0/0
9718.9596	Ti I	1.5025	-1.181	-0.21	0.42	0/2
9728.4069	Ti I	0.8181	-1.206	(s)	(s)	0/0
9730.3160	Cr I	3.5505	-0.770	-0.58	0.65	0/2
9734.5630	Cr I	2.5438	-1.950	-0.06	0.70:	1/2
9738.5725	Fe I	4.9913	0.150	-0.54	0.00	0/2
9743.6059	Ti I	0.8129	-1.306	(s)	(s)	0/0
9753.0906	Fe I	4.7955	-0.782	-0.60	-0.30	0/2
9770.3011	Ti I	0.8484	-1.581	(s)	(s)	0/0
9773.3530	Cr I	3.5561	-1.559	(w)	-0.04	0/1
9787.6874	Ti I	0.8259	-1.444	(s)	(b)	0/0
9791.6983	Fe I	2.9904	-4.223	(w)	-0.30	0/1
9800.3075	Fe I	5.0856	-0.453	-0.96	-0.16	0/2
9811.5041	Fe I	5.0117	-1.362	-0.37	0.34	0/2
9820.2408	Fe I	2.4242	-5.073	(w)	0.03	0/1
9828.1320	Mg I	5.9328	-1.890	-0.81	0.71:	1/2
9832.1397	Ti I	1.8871	-1.130	-0.21	(b)	0/1
9861.7337	Fe I	5.0638	-0.142	-0.79	(b)	0/1
9868.1857	Fe I	5.0856	-0.979	-0.40	0.67	0/2
9879.5830	Ti I	1.8732	-2.400	-0.22	0.12	0/2

Table 1 *continued***Table 1** (*continued*)

λ_{air} (Å)	Atom	EP (eV)	$\log gf$ (dex)	Arcturus (dex)	μ Leo (dex)	flag
9889.0351	Fe I	5.0331	-0.446	-0.45	0.30	0/2
9927.3506	Ti I	1.8792	-1.290	-0.30	0.41	0/2
9937.0898	Fe I	4.5931	-2.442	(w)	0.12	0/1
9944.2065	Fe I	5.0117	-1.338	-0.39	0.10	0/2
9969.1321	Si I	6.0787	-1.996	(w)	0.04	0/1
9980.4629	Fe I	5.0331	-1.379	-0.52	0.53	0/2
9983.1880	Mg I	5.9315	-2.153	-0.07	0.31	0/2
9997.9591	Ti I	1.8732	-1.560	-0.17	0.23	0/2
10003.088	Ti I	2.1603	-1.210	-0.26	0.37	0/2
10005.664	Ti I	1.0666	-3.650	(w)	0.32	0/1
10011.744	Ti I	2.1535	-1.390	-0.18	0.47	0/2
10034.491	Ti I	1.4601	-1.770	-0.22	0.47	0/2
10041.472	Fe I	5.0117	-1.772	(w)	0.48	0/1
10059.904	Ti I	1.4298	-2.080	-0.30	0.33	0/2
10061.245	Ni I	5.4943	-0.401	(w)	-0.11	0/1
10065.045	Fe I	4.8349	-0.289	-0.62	0.26	0/2
10066.512	Ti I	2.1603	-1.850	-0.09	0.50	0/2
10068.329	Si I	6.0986	-1.318	-0.34	0.04	0/2
10080.350	Cr I	3.5558	-1.272	(b)	0.21	0/1
10081.393	Fe I	2.4242	-4.537	-0.41	0.31	0/2
10083.180	Cr I	3.5561	-1.720	(w)	-0.14	0/1
10114.014	Fe I	2.7586	-3.692	-0.62	(b)	0/1
10124.930	Si I	6.1248	-2.035	(w)	0.50	0/1
10145.561	Fe I	4.7955	-0.177	-0.60	(b)	0/1
10155.162	Fe I	2.1759	-4.226	-0.63	0.18	0/2
10167.468	Fe I	2.1979	-4.117	-0.55	0.35	0/2
10189.146	Ti I	1.4601	-3.100	(w)	0.48	0/1
10193.224	Ni I	4.0893	-0.656	-0.58	0.43	0/2
10195.105	Fe I	2.7275	-3.580	-0.57	0.38	0/2
10216.313	Fe I	4.7331	-0.063	-0.55	0.40	0/2
10218.408	Fe I	3.0713	-2.760	-0.57	0.58	0/2
10227.994	Fe I	6.1189	-0.354	(w)	0.43	0/1
10265.217	Fe I	2.2227	-4.537	-0.61	0.07	0/2
10273.684	Ca I	4.5347	-0.636	-0.33	-0.44:	1/2
10288.944	Si I	4.9201	-1.511	-0.54	0.26	0/2
10299.290	Mg I	6.1182	-2.076	-0.13	-0.73:	1/2

Table 1 *continued*

Table 1 (continued)

λ_{air}	Atom	EP	$\log gf$	Arcturus	μ Leo	flag
(Å)		(eV)	(dex)	(dex)	(dex)	
10302.611	Ni I	4.2661	-0.881	-0.64	0.38	0/2
10307.454	Fe I	4.5931	-2.067	-0.94	-0.20	0/2
10312.531	Mg I	6.1182	-1.730	0.00	0.49	0/2
10313.197	Si I	6.3991	-0.886	-0.52	0.32	0/2
10330.228	Ni I	4.1054	-0.982	-0.53	0.69	0/2
10340.885	Fe I	2.1979	-3.577	-0.50	0.31	0/2
10343.819	Ca I	2.9325	-0.300	(s)	(s)	0/0
10347.965	Fe I	5.3933	-0.551	-0.74	0.39	0/2
10353.804	Fe I	5.3933	-0.819	-0.69	0.16	0/2
10360.578	Fe I	5.5188	-1.403	(w)	-0.51	0/1
10371.263	Si I	4.9296	-0.705	-0.33	0.24	0/2
10388.744	Fe I	5.4457	-1.468	(w)	0.38	0/1
10395.794	Fe I	2.1759	-3.393	-0.57	0.13	0/2
10396.802	Ti I	0.8484	-1.539	(s)	(s)	0/0
10407.037	Si I	6.6161	-0.597	-0.5:	(*)	1/1
10414.913	Si I	6.6192	-1.137	(w)	-0.26	0/1
10416.620	Cr I	3.0128	-2.508	(w)	0.16	0/1
10435.355	Fe I	4.7331	-1.945	(w)	0.39	0/1
10469.652	Fe I	3.8835	-1.184	-0.62	0.48	0/2
10486.250	Cr I	3.0106	-0.949	-0.62	0.42	0/2
10496.113	Ti I	0.8360	-1.651	(s)	(s)	0/0
10510.010	Cr I	3.0133	-1.535	-0.71	0.08	0/2
10517.511	Si I	6.7271	-1.038	(w)	0.04	0/1
10530.514	Ni I	4.1054	-1.189	-0.49	0.55	0/2
10532.234	Fe I	3.9286	-1.480	-0.64	0.19	0/2
10535.709	Fe I	6.2057	-0.108	(w)	0.33	0/1
10550.100	Cr I	3.0111	-2.629	(w)	0.41	0/1
10555.649	Fe I	5.4457	-1.108	(w)	-0.09	0/1
10565.952	Ti I	2.2363	-1.777	-0.6:	0.07	1/2
10577.139	Fe I	3.3014	-3.136	-0.57	0.53	0/2
10582.160	Si I	6.2227	-1.169	-0.24	0.30	0/2
10585.141	Si I	4.9538	0.012	(s)	(s)	0/0
10603.425	Si I	4.9296	-0.305	(s)	(s)	0/0
10607.718	Ti I	0.8484	-2.697	-0.41	0.20	0/2
10611.686	Fe I	6.1692	0.021	-0.56	0.56	0/2
10616.721	Fe I	3.2671	-3.127	-0.72	0.09	0/2
10627.648	Si I	5.8625	-0.866	0.44:	1.32:	2/2
10647.640	Cr I	3.0106	-1.582	-0.70	0.19	0/2
10660.973	Si I	4.9201	-0.266	(s)	(s)	0/0
10667.520	Cr I	3.0128	-1.481	-0.79	0.11	0/2

Table 1 continued

Table 1 (continued)

λ_{air}	Atom	EP	$\log gf$	Arcturus	μ Leo	flag
(Å)		(eV)	(dex)	(dex)	(dex)	
10672.140	Cr I	3.0133	-1.354	-0.67	0.35	0/2
10674.070	Fe I	6.1692	-0.466	(w)	0.42	0/1
10677.047	Ti I	0.8360	-2.522	-0.38	0.19	0/2
10689.716	Si I	5.9537	-0.120	-0.03	0.64	0/2
10694.251	Si I	5.9639	0.048	-0.10	0.71	0/2
10717.806	Fe I	5.5392	-0.436	-1.55:	-0.89:	2/2
10725.185	Fe I	3.6398	-2.763	-0.73	0.19	0/2
10726.391	Ti I	0.8129	-2.064	-0.20	0.51	0/2
10727.406	Si I	5.9840	0.217	-0.07	0.63	0/2
10732.864	Ti I	0.8259	-2.515	-0.27	0.47	0/2
10749.378	Si I	4.9296	-0.205	(s)	(s)	0/0
10753.004	Fe I	3.9597	-1.845	-0.77	0.18	0/2
10762.255	Ni I	4.1536	-2.165	(w)	0.97:	1/1
10770.134	Si I	6.6192	-1.253	(w)	0.46	0/1
10771.228	Fe I	5.5869	-1.285	(w)	-0.24	0/1
10774.866	Ti I	0.8181	-2.666	-0.30	0.34	0/2
10780.694	Fe I	3.2367	-3.289	-0.84	-0.08	0/2
10783.050	Fe I	3.1110	-2.567	-0.71	0.09	0/2
10784.562	Si I	5.9639	-0.839	-0.18	0.40	0/2
10786.849	Si I	4.9296	-0.303	(s)	(s)	0/0
10796.106	Si I	6.1807	-1.266	-0.41	0.30	0/2
10801.360	Cr I	3.0111	-1.562	-0.80	0.26	0/2
10816.910	Cr I	3.0128	-1.894	-0.54	0.38	0/2
10818.274	Fe I	3.9597	-1.948	-0.67	0.48	0/2
10821.660	Cr I	3.0133	-1.520	-0.71	0.06	0/2
10827.088	Si I	4.9538	0.302	(s)	(s)	0/0
10838.970	Ca I	4.8775	0.238	-0.41	0.28	0/2
10843.858	Si I	5.8625	-0.112	0.11	0.80	0/2
10847.633	Ti I	0.8259	-3.922	-0.65:	-0.48:	2/2
10861.582	Ca I	4.8767	-0.343	(w)	0.23	0/1
10863.518	Fe I	4.7331	-0.895	-0.67	0.24	0/2
10869.536	Si I	5.0823	0.371	(s)	(s)	0/0
10881.758	Fe I	2.8450	-3.604	-0.44	0.59	0/2
10882.809	Si I	5.9840	-0.815	(b)	0.31	0/1
10884.262	Fe I	3.9286	-1.925	-0.70	0.10	0/2
10885.333	Si I	6.1807	0.221	-0.37	0.40	0/2
10891.307	Ni I	4.1672	-1.246	-0.47	(b)	0/1
10896.299	Fe I	3.0713	-2.694	-0.83	0.01	0/2
10905.710	Cr I	3.4379	-0.561	-0.52	0.31	0/2
10953.320	Mg I	5.9315	-0.863	0.03	0.48	0/2

Table 1 continued

Table 1 (continued)

λ_{air}	Atom	EP	$\log gf$	Arcturus	μ Leo	flag
(Å)		(eV)	(dex)	(dex)	(dex)	
10979.308	Si I	4.9538	-0.524	-0.07	(s)	0/1
10982.058	Si I	6.1910	0.104	-0.42	0.17	0/2
11026.788	Fe I	3.9433	-2.805	-0.42	0.21	0/2
11053.512	Fe I	3.9841	-3.311	(w)	0.23	0/1
11119.795	Fe I	2.8450	-2.202	(s)	(s)	0/0
11130.028	Si I	6.2060	-0.194	-0.19	0.07	0/2
11135.958	Fe I	5.3139	-1.718	(w)	0.96:	1/1
11607.572	Fe I	2.1979	-2.009	(s)	(s)	0/0
11638.260	Fe I	2.1759	-2.214	(s)	(s)	0/0
11640.941	Si I	6.2739	-0.432	-0.20	0.26	0/2
11681.594	Fe I	3.5465	-3.615	(w)	0.26	0/1
11689.972	Fe I	2.2227	-2.068	(s)	(b)	0/0
11715.486	Fe I	5.6424	-1.362	(w)	0.57	0/1
11725.562	Fe I	5.6989	-1.096	(w)	-0.23	0/1
11759.570	Ca I	4.5313	-0.878	(w)	0.13	0/1
11767.481	Ca I	4.5322	-0.536	-0.48	0.28	0/2
11780.542	Ti I	1.4432	-2.170	-0.31	-0.02	0/2
11783.265	Fe I	2.8316	-1.574	(s)	(s)	0/0
11793.043	Ca I	4.5347	-0.258	-0.22	0.55	0/2
11797.186	Ti I	1.4298	-2.280	-0.31	0.17	0/2
11828.171	Mg I	4.3458	-0.333	(s)	(s)	0/0
11854.238	Fe I	5.6826	-1.306	(w)	-0.23	0/1
11863.920	Si I	5.9840	-1.457	-0.28	0.30	0/2
11892.877	Ti I	1.4298	-1.730	-0.13	(b)	0/1
11900.055	Si I	5.9639	-1.864	-0.03	0.57	0/2
11927.838	Ni I	4.2661	-2.105	(w)	-0.33	1/1
11955.955	Ca I	4.1308	-0.849	-0.37	0.29	0/2
11973.046	Fe I	2.1759	-1.483	(s)	(s)	0/0
11984.198	Si I	4.9296	0.239	(s)	(s)	0/0
11991.568	Si I	4.9201	-0.109	(s)	(s)	0/0
12000.970	Cr I	3.4348	-2.068	(w)	0.06	0/1
12031.504	Si I	4.9538	0.477	(s)	(s)	0/0
12039.822	Mg I	5.7532	-1.530	-0.14	0.21	0/2
12053.082	Fe I	4.5585	-1.543	-0.63	0.05	0/2
12103.534	Si I	4.9296	-0.350	(s)	(s)	0/0
12105.841	Ca I	4.5541	-0.305	-0.48	0.06	0/2
12110.659	Si I	6.6161	-0.136	-0.53	0.38	0/2
12119.494	Fe I	4.5931	-1.635	-0.69	0.18	0/2
12175.733	Si I	6.6192	-0.855	-0.28	0.41	0/2
12178.339	Si I	6.2694	-1.100	-0.15	0.56	0/2

Table 1 continued

Table 1 (continued)

λ_{air}	Atom	EP	$\log gf$	Arcturus	μ Leo	flag
(Å)		(eV)	(dex)	(dex)	(dex)	
12190.098	Fe I	3.6352	-2.330	-0.79	0.22	0/2
12213.336	Fe I	4.6382	-1.845	-0.55	0.34	0/2
12216.579	Ni I	5.2825	-0.513	-0.46	0.41	0/2
12227.112	Fe I	4.6070	-1.368	-0.80	-0.01	0/2
12255.699	Ti I	3.9215	0.161	(w)	-0.04	0/1
12270.692	Si I	4.9538	-0.396	(s)	(s)	0/0
12283.298	Fe I	6.1692	-0.537	(w)	0.27	0/1
12340.481	Fe I	2.2786	-5.098	-0.24	0.55	1/2
12342.916	Fe I	4.6382	-1.463	-0.71	0.36	0/2
12390.154	Si I	5.0823	-1.767	-0.42	0.37	0/2
12395.832	Si I	4.9538	-1.644	-0.44	0.28	0/2
12417.937	Mg I	5.9315	-1.664	-0.21	0.26	0/2
12423.029	Mg I	5.9320	-1.188	-0.25	(b)	0/1
12433.452	Mg I	5.9328	-0.967	-0.43	(b)	0/1
12457.132	Mg I	6.4314	-2.260	(w)	0.87	1/1
12532.840	Cr I	2.7088	-1.879	-0.62	0.28	0/2
12556.996	Fe I	2.2786	-3.626	-0.82	-0.19	0/2
12583.924	Si I	6.6161	-0.462	-0.40	0.12	0/2
12589.204	Si I	6.6161	-1.507	(w)	(b)	0/0
12600.277	Ti I	1.4432	-2.320	-0.32	0.10	0/2
12615.928	Fe I	4.6382	-1.517	-0.83	0.21	0/2
12627.674	Si I	6.6192	-0.805	-0.47	0.09	0/2
12638.703	Fe I	4.5585	-0.783	-0.72	0.22	0/2
12648.741	Fe I	4.6070	-1.140	-0.63	0.08	0/2
12671.096	Ti I	1.4298	-2.360	-0.26	0.49	0/2
12738.383	Ti I	2.1747	-1.280	-0.26	0.27	0/2
12743.264	Ni I	5.2843	-0.452	-0.80	-0.37	1/2
12744.905	Ti I	2.4875	-1.280	-0.32	0.01	0/2
12789.450	Fe I	5.0095	-1.514	-0.72	0.03	0/2
12807.152	Fe I	3.6398	-2.452	-0.61	0.26	0/2
12811.478	Ti I	2.1603	-1.390	-0.23	0.37	0/2
12816.045	Ca I	3.9104	-0.765	0.17	0.82	2/2
12821.672	Ti I	1.4601	-1.190	-0.05	0.82	1/2
12823.867	Ca I	3.9104	-0.997	-0.42	(b)	0/1
12824.859	Fe I	3.0176	-3.835	-0.22	(b)	1/1
12827.059	Ca I	3.9104	-1.478	-0.33	0.31	0/2
12831.445	Ti I	1.4298	-1.490	-0.09	0.84	0/2
12840.574	Fe I	4.9556	-1.329	-0.81	(b)	0/1
12847.034	Ti I	1.4432	-1.330	-0.19	0.47	0/2
12870.041	Mg I	6.5879	-1.530	-0.33	0.26	0/2

Table 1 continued

Table 1 (*continued*)

λ_{air}	Atom	EP	$\log gf$	Arcturus	μ Leo	flag
(Å)		(eV)	(dex)	(dex)	(dex)	
12879.766	Fe I	2.2786	-3.458	-0.63	0.17	0/2
12885.290	Ca I	4.4300	-1.164	(w)	0.07	0/1
12896.118	Fe I	4.9130	-1.424	-0.74	-0.01	0/2
12910.090	Cr I	2.7079	-1.779	-0.58	0.23	0/2
12919.899	Ti I	2.1535	-1.560	-0.37	0.33	0/2
12921.810	Cr I	2.7088	-2.743	(w)	0.18	0/1
12927.477	Ti I	2.1535	-2.440	(w)	-0.27	0/1
12932.313	Ni I	2.7403	-2.523	-0.93	-0.02	0/2
12937.020	Cr I	2.7099	-1.896	-0.66	0.07	0/2
12950.896	Ti I	3.4406	-0.569	(w)	0.44	0/1
12987.567	Ti I	2.5057	-1.550	-0.30	0.20	0/2
13006.684	Fe I	2.9904	-3.744	-0.24	0.93	2/2
13011.897	Ti I	1.4432	-2.270	-0.30	0.42	0/2
13014.841	Fe I	5.4457	-1.693	(w)	0.46	0/1
13033.554	Ca I	4.4410	-0.064	-0.48	0.23	0/2
13039.647	Fe I	5.6547	-0.731	-0.96	-0.47	0/2
13048.181	Ni I	4.5379	-1.008	-0.65	0.34	0/2
13077.265	Ti I	1.4601	-2.220	-0.24	(b)	0/1
13086.027	Si I	6.0827	-1.412	-0.62	(b)	0/1
13098.876	Fe I	5.0095	-1.290	-0.83	-0.06	0/2
13102.057	Si I	6.0827	-0.309	-0.35	-0.07	0/2
13107.972	Fe I	5.6693	-1.449	(w)	-0.37	0/1
13134.942	Ca I	4.4506	0.085	-0.37	0.44	0/2
13145.071	Fe I	4.1426	-3.296	(w)	0.30	0/1
13147.920	Fe I	5.3933	-0.814	-0.49	0.25	0/2
13152.743	Si I	4.9201	-2.504	-0.26	0.08	0/2
13176.888	Si I	5.8625	-0.200	-0.07	0.75	0/2
13201.150	Cr I	2.7088	-1.834	-0.59	0.25	0/2
13212.418	Ni I	2.7403	-3.901	(w)	(b)	0/0
13217.020	Cr I	2.7099	-2.302	-0.59	0.65	0/2
13222.523	Fe I	5.6547	-1.278	(w)	0.03	0/1
13255.812	Ti I	2.2312	-2.119	-0.27	0.13	0/2

NOTE— Here presented is the entire table which is also available as an online material on the journal website.

Table 2. Lines Selected from MB99 and Abundances

λ_{air} (Å)	Atom	EP (eV)	$\log gf$ (dex)	Arcturus (dex)	μ Leo (dex)	flag
10003.09	Ti I	2.16	-1.32	-0.22	0.19	0/2
10011.74	Ti I	2.15	-1.54	-0.03	(b)	0/1
10013.86	Si I	6.40	-1.73	(w)	-0.17	0/1
10019.79	Fe I	5.48	-1.44	(w)	0.30	0/1
10032.86	Fe I	5.51	-1.36	(w)	0.26	0/1
10034.49	Ti I	1.46	-2.09	0.12	0.65	0/2
10041.47	Fe I	5.01	-1.84	(w)	0.51	0/1
10059.90	Ti I	1.43	-2.40	0.02	0.54	0/2
10065.05	Fe I	4.84	-0.57	-0.25	0.52	0/2
10066.55	Ti I	2.16	-1.85	-0.10	0.47	0/2
10068.37	Si I	6.10	-1.40	-0.24	-0.12	0/2
10080.30	Cr I	3.56	-1.45	(w)	0.30	0/1
10081.39	Fe I	2.42	-4.53	-0.43	0.18	0/2
10098.55	Si I	6.40	-1.76	(w)	0.44	0/1
10114.02	Fe I	2.76	-3.76	-0.52	(b)	0/1
10145.57	Fe I	4.80	-0.41	-0.24	0.51	0/2
10155.16	Fe I	2.18	-4.36	-0.49	0.17	0/2
10167.47	Fe I	2.20	-4.26	-0.39	0.34	0/2
10189.13	Ti I	1.46	-3.27	(w)	0.61	0/1
10193.23	Ni I	4.09	-0.81	-0.37	0.50	0/2
10195.11	Fe I	2.73	-3.63	-0.51	0.27	0/2
10197.01	Cr I	2.99	-2.44	(w)	-0.04	0/1
10216.32	Fe I	4.73	-0.29	-0.2:	0.62	1/2
10218.41	Fe I	3.07	-2.93	-0.38	0.55	0/2
10230.78	Fe I	5.87	-0.70	(w)	0.40	0/1
10249.15	Ca I	4.53	-0.96	(w)	0.40	0/1
10254.77	Ca I	4.53	-0.98	(w)	0.46	0/1
10265.22	Fe I	2.22	-4.67	-0.47	0.13	0/2
10273.69	Ca I	4.53	-0.76	(w)	0.16	0/1
10288.94	Si I	4.92	-1.71	-0.31	0.41	0/2
10299.24	Mg I	6.12	-2.06	(b)	-0.83:	1/1
10301.41	Si I	6.10	-1.83	(w)	0.44	0/1
10307.45	Fe I	4.59	-2.45	(w)	0.17	0/1
10312.52	Mg I	6.12	-1.71	-0.17	0.25	0/2
10340.89	Fe I	2.20	-3.65	-0.40	0.16	0/2
10343.83	Ca I	2.93	-0.40	(s)	(s)	0/0
10347.96	Fe I	5.39	-0.82	-0.47	0.57	0/2
10353.81	Fe I	5.39	-1.09	(w)	0.33	0/1

Table 2 *continued***Table 2** (*continued*)

λ_{air} (Å)	Atom	EP (eV)	$\log gf$ (dex)	Arcturus (dex)	μ Leo (dex)	flag
10371.27	Si I	4.93	-0.80	-0.06	0.40	0/2
10395.80	Fe I	2.18	-3.42	-0.61	-0.03	0/2
10396.81	Ti I	0.85	-1.79	(s)	0.71	0/1
10401.72	Fe I	3.02	-4.36	(w)	0.25	0/1
10406.96	Si I	6.62	-0.77	-0.38	-0.14	0/2
10414.85	Si I	6.62	-1.38	(w)	0.25	0/1
10416.65	Cr I	3.01	-2.40	(w)	-0.10	0/1
10435.36	Fe I	4.73	-2.11	(w)	0.45	0/1
10452.75	Fe I	3.88	-2.30	-0.67	0.27	0/2
10469.66	Fe I	3.88	-1.37	-0.43	0.42	0/2
10481.27	Ca I	4.74	-0.83	(w)	0.35	0/1
10486.22	Cr I	3.01	-1.16	-0.40	0.46	0/2
10496.09	Ti I	0.84	-1.91	(s)	0.49	0/1
10509.99	Cr I	3.01	-1.78	-0.47	0.26	0/2
10516.14	Ca I	4.74	-0.52	(w)	0.25	0/1
10530.52	Ni I	4.11	-1.30	-0.36	0.58:	1/2
10532.24	Fe I	3.93	-1.76	-0.35	0.27	0/2
10550.06	Cr I	3.01	-2.66	(w)	0.47	0/1
10555.65	Fe I	5.45	-1.39	(w)	0.16	0/1
10565.97	Ti I	2.24	-2.10	(w)	0.37	0/1
10577.14	Fe I	3.30	-3.28	-0.42	0.55	0/2
10582.17	Si I	6.22	-1.16	-0.27	0.24	0/2
10585.14	Si I	4.95	-0.06	(b)	(s)	0/0
10603.44	Si I	4.93	-0.37	0.21	(s)	0/1
10607.73	Ti I	0.85	-3.16	0.07	0.56	0/2
10611.68	Fe I	6.17	-0.09	-0.44	0.63	0/2
10616.72	Fe I	3.27	-3.34	-0.52	0.19	0/2
10627.65	Si I	5.86	-0.50	0.09	0.86	0/2
10647.65	Cr I	3.01	-1.78	-0.54	0.24	0/2
10660.97	Si I	4.92	-0.32	(s)	(s)	0/0
10661.63	Ti I	0.82	-2.07	-0.12	(b)	0/1
10667.52	Cr I	3.01	-1.69	-0.51	0.39	0/2
10672.14	Cr I	3.01	-1.57	-0.46	0.41	0/2
10677.05	Ti I	0.84	-2.90	0.02	0.45	0/2
10689.72	Si I	5.95	-0.09	0.06	0.73	0/2
10694.26	Si I	5.96	0.10	-0.09	0.62	0/2
10725.19	Fe I	3.64	-2.98	-0.54	0.33	0/2
10726.39	Ti I	0.81	-2.31	0.02	0.49	0/2
10727.42	Si I	5.98	0.29	-0.19	0.42	0/2
10732.87	Ti I	0.83	-2.82	0.01	0.54	0/2

Table 2 *continued*

Table 2 (*continued*)

λ_{air}	Atom	EP	$\log gf$	Arcturus	μ Leo	flag
(Å)		(eV)	(dex)	(dex)	(dex)	
10749.39	Si I	4.93	-0.21	(s)	(s)	0/0
10753.01	Fe I	3.96	-2.14	-0.48	0.29	0/2
10754.76	Fe I	2.83	-4.39	-0.51	0.22	0/2
10774.87	Ti I	0.82	-2.98	0.01	0.45	0/2
10780.70	Fe I	3.24	-3.59	-0.55	0.20	0/2
10783.05	Fe I	3.11	-2.80	-0.51	-0.01	0/2
10784.56	Si I	5.96	-0.72	-0.33	0.18	0/2
10786.87	Si I	4.93	-0.38	(s)	(s)	0/0
10791.45	Ca I	4.74	-0.68	(w)	0.47	0/1
10792.51	Ti I	0.85	-3.80	-0.95:	-0.17	1/2
10796.11	Si I	6.18	-1.49	-0.20	0.47	0/2
10801.36	Cr I	3.01	-1.77	-0.59	0.38	0/2
10809.08	Ca I	4.68	-1.08	(w)	(b)	0/0
10816.90	Cr I	3.01	-2.01	-0.40	0.50	0/2
10818.28	Fe I	3.96	-2.23	-0.39	0.56	0/2
10821.68	Cr I	3.01	-1.73	(b)	0.26	0/1
10827.10	Si I	4.95	0.23	(s)	(s)	0/0
10833.38	Ca I	4.88	-0.43	(w)	0.30	0/1
10838.98	Ca I	4.88	0.03	-0.21	0.30	0/2
10843.86	Si I	5.86	-0.05	0.14	0.73	0/2
10846.79	Ca I	4.74	-0.64	(w)	0.48	0/1
10849.46	Fe I	5.54	-0.73	-0.46	0.37	0/2
10853.00	Fe I	3.87	-3.27	(w)	0.53	0/1
10861.59	Ca I	4.88	-0.49	(w)	0.34	0/1
10863.52	Fe I	4.73	-1.06	-0.44	0.35	0/2
10869.54	Si I	5.08	0.36	(s)	(s)	0/0
10879.88	Ca I	4.88	-0.51	(w)	0.08	0/1
10881.76	Fe I	2.85	-3.50	-0.48	0.36	0/2
10882.81	Si I	5.98	-0.62	-0.33	0.11	0/2
10884.26	Fe I	3.93	-2.18	-0.51	0.11	0/2
10885.35	Si I	6.18	-0.10	-0.14	0.58	0/2
10896.30	Fe I	3.07	-2.93	-0.51	0.27	0/2
10905.72	Cr I	3.44	-0.70	-0.30	0.48	0/2
10953.32	Mg I	5.93	-0.90	0.08	0.43	0/2
10979.31	Si I	4.95	-0.60	0.29	(s)	0/1
10982.08	Si I	6.19	-0.27	-0.08	0.55	0/2
11015.53	Cr I	3.45	-0.58	-0.22:	0.53	1/2
11026.78	Fe I	3.94	-2.77	-0.47	0.10	0/2
11053.52	Fe I	3.98	-3.09	(w)	-0.07	0/1
11119.80	Fe I	2.85	-2.54	-0.46	(b)	0/1

Table 2 *continued***Table 2** (*continued*)

λ_{air}	Atom	EP	$\log gf$	Arcturus	μ Leo	flag
(Å)		(eV)	(dex)	(dex)	(dex)	
11130.03	Si I	6.21	-0.31	-0.06	0.14	0/2
11135.96	Fe I	5.31	-1.10	-0.31	0.25	0/2
11607.57	Fe I	2.20	-2.46	(s)	(s)	0/0
11638.26	Fe I	2.18	-2.59	(s)	(s)	0/0
11640.96	Si I	6.27	-0.48	-0.17	0.24	0/2
11681.60	Fe I	3.55	-3.41	-0.64	0.13	0/2
11700.27	Si I	6.27	-0.67	0.04	1.45:	1/2
11715.49	Fe I	5.64	-1.20	(w)	0.35	0/1
11780.55	Ti I	1.44	-2.42	-0.06	0.19	0/2
11783.26	Fe I	2.83	-1.86	(s)	(s)	0/0
11797.18	Ti I	1.43	-2.33	-0.24	0.22	0/2
11828.19	Mg I	4.35	-0.50	(s)	(s)	0/0
11863.92	Si I	5.98	-1.50	-0.24	0.30	0/2
11892.89	Ti I	1.43	-1.73	-0.12	0.29	0/2
11900.03	Si I	5.96	-1.79	-0.11	0.48	0/2
11927.84	Ni I	4.27	-2.26	(w)	-0.23	0/1
11955.95	Ca I	4.13	-0.91	-0.31	0.30	0/2
11973.04	Fe I	2.18	-2.28	(s)	(s)	0/0
11984.23	Si I	4.93	0.12	(s)	(s)	0/0
11991.58	Si I	4.92	-0.22	(s)	(s)	0/0
12000.97	Cr I	3.44	-1.93	(w)	-0.09	0/1
12031.53	Si I	4.95	0.24	(s)	(s)	0/0
12039.84	Mg I	5.75	-1.55	-0.13	0.16	0/2
12053.08	Fe I	4.56	-1.75	-0.40	0.20	0/2
12103.54	Si I	4.93	-0.49	0.28	(s)	0/1
12105.84	Ca I	4.55	-0.54	-0.22	0.34	0/2
12119.50	Fe I	4.59	-1.88	-0.46	0.34	0/2
12133.99	Si I	5.98	-1.89	-0.24	0.36	0/2
12175.75	Si I	6.62	-0.97	-0.17	0.49	0/2
12178.40	Si I	6.27	-1.14	-0.10	0.61	0/2
12190.10	Fe I	3.63	-2.75	-0.39	0.45	0/2
12196.70	Si I	5.08	-3.27	(w)	-0.19	0/1
12213.34	Fe I	4.64	-2.09	-0.30	0.53	0/2
12227.12	Fe I	4.61	-1.60	-0.55	0.17	0/2
12255.70	Ti I	3.92	-0.07	(w)	0.20	0/1
12270.71	Si I	4.95	-0.54	0.16	(s)	0/1
12283.28	Fe I	6.17	-0.61	(w)	0.28	0/1
12340.49	Fe I	2.28	-4.79	-0.56	0.15	0/2
12342.92	Fe I	4.64	-1.68	-0.47	0.48	0/2
12388.37	Ti I	2.16	-1.81	-0.93:	0.11	1/2

Table 2 *continued*

Table 2 (*continued*)

λ_{air}	Atom	EP	$\log gf$	Arcturus	μ Leo	flag
(Å)		(eV)	(dex)	(dex)	(dex)	
12390.17	Si I	5.08	-1.93	-0.24	0.46	0/2
12395.84	Si I	4.95	-1.82	-0.23	0.41	0/2
12417.92	Mg I	5.93	-1.69	-0.18	0.26	0/2
12423.02	Mg I	5.93	-1.23	-0.18	0.17	0/2
12433.45	Mg I	5.93	-1.00	-0.23	0.15	0/2
12449.42	Ni I	6.10	-0.01	(w)	-0.03	0/1
12460.70	Ti I	4.24	0.78	-0.72:	0.11	1/2
12532.85	Cr I	2.71	-2.07	-0.43	0.36	0/2
12557.01	Fe I	2.28	-4.07	-0.36	0.06	0/2
12583.95	Si I	6.62	-0.62	-0.23	0.30	0/2
12589.21	Si I	6.62	-1.56	(w)	0.35	0/1
12600.27	Ti I	1.44	-2.48	-0.19	0.16	0/2
12615.93	Fe I	4.64	-1.77	-0.56	0.40	0/2
12627.70	Si I	6.62	-1.07	-0.22	0.33	0/2
12638.72	Fe I	4.56	-1.00	-0.39	0.49	0/2
12648.74	Fe I	4.61	-1.32	-0.39	0.20	0/2
12671.10	Ti I	1.43	-2.19	-0.40	0.31	0/2
12738.39	Ti I	2.71	-0.90	0.10	0.51	0/2
12743.26	Ni I	5.28	-0.91	(w)	0.07	0/1
12744.91	Ti I	2.49	-1.54	-0.04	0.32	0/2
12789.47	Fe I	5.01	-1.92	(w)	0.39	0/1
12807.16	Fe I	3.64	-2.76	-0.29	0.45	0/2
12811.48	Ti I	2.16	-1.60	-0.01	0.50	0/2
12816.05	Ca I	3.91	-1.27	0.82:	1.19:	2/2
12821.67	Ti I	1.46	-1.67	0.44:	1.02	1/2
12824.87	Fe I	3.02	-3.68	-0.47	0.05	0/2
12827.02	Ca I	3.91	-1.70	(w)	0.52	0/1
12831.41	Ti I	1.43	-1.85	0.29	0.97	0/2
12840.58	Fe I	4.95	-1.76	-0.23	(b)	0/1
12847.05	Ti I	1.44	-1.71	0.21	0.65	0/2
12879.78	Fe I	2.28	-3.61	-0.44	0.13	0/2
12896.12	Fe I	4.91	-1.80	-0.37	0.30	0/2
12910.10	Cr I	2.71	-1.99	-0.46	0.27	0/2
12919.90	Ti I	2.15	-1.74	-0.19	0.45	0/2
12921.81	Cr I	2.71	-2.73	(w)	0.20	0/1
12937.03	Cr I	2.71	-2.09	-0.48	0.15	0/2
12946.54	Fe I	3.25	-4.23	(w)	-0.01	0/1
12950.90	Ti I	3.44	-0.54	(w)	0.40	0/1
13001.42	Ca I	4.44	-1.24	(w)	-0.08	0/1
13006.70	Fe I	2.99	-3.49	-0.53	0.42	0/2

Table 2 *continued***Table 2** (*continued*)

λ_{air}	Atom	EP	$\log gf$	Arcturus	μ Leo	flag
(Å)		(eV)	(dex)	(dex)	(dex)	
13011.90	Ti I	1.44	-2.50	-0.10	0.55	0/2
13014.85	Fe I	5.45	-1.68	(w)	0.30	0/1
13033.56	Ca I	4.44	-0.31	-0.23	0.36	0/2
13039.66	Fe I	5.66	-1.32	(w)	0.09	0/1
13077.27	Ti I	1.46	-2.34	-0.10	(b)	0/1
13086.44	Ca I	4.44	-0.90	-0.36	0.25	0/2
13098.92	Fe I	5.01	-1.73	-0.38	0.37	0/2
13102.07	Si I	6.08	-0.72	0.06	0.30	0/2
13134.94	Ca I	4.45	-0.14	-0.16	0.46	0/2
13147.93	Fe I	5.39	-0.93	-0.34	0.34	0/2
13152.74	Si I	4.92	-2.58	-0.22	0.04	0/2
13167.78	Ca I	4.45	-1.23	(w)	0.19	0/1
13176.91	Si I	5.86	-0.30	0.09	0.80	0/2
13201.16	Cr I	2.71	-2.08	-0.34	0.37	0/2
13212.45	Ni I	2.74	-3.04	-0.10	0.8:	1/2
13217.02	Cr I	2.71	-2.52	-0.38	0.73	0/2
13264.17	Ni I	5.28	-1.03	(w)	-0.27	0/1
13291.78	Fe I	5.48	-1.58	(w)	0.25	0/1

NOTE— Here presented is the entire table which is also available as an online material on the journal website.